Foreign Object Damage in Disks of Two Gas-Turbine-Grade Silicon Nitrides by Steel Ball Projectiles at Ambient Temperature

Sung R. Choi
Ohio Aerospace Institute, Brook Park, Ohio

J. Michael Pereira, Lesley A. Janosik, and Ramakrishna T. Bhatt
Glenn Research Center, Cleveland, Ohio

Since its founding, NASA has been dedicated to the advancement of aeronautics and space science. The NASA Scientific and Technical Information (STI) Program Office plays a key part in helping NASA maintain this important role.

The NASA STI Program Office is operated by Langley Research Center, the Lead Center for NASA's scientific and technical information. The NASA STI Program Office provides access to the NASA STI Database, the largest collection of aeronautical and space science STI in the world. The Program Office is also NASA's institutional mechanism for disseminating the results of its research and development activities. These results are published by NASA in the NASA STI Report Series, which includes the following report types:

- TECHNICAL PUBLICATION. Reports of completed research or a major significant phase of research that present the results of NASA programs and include extensive data or theoretical analysis. Includes compilations of significant scientific and technical data and information deemed to be of continuing reference value. NASA's counterpart of peer-reviewed formal professional papers but has less stringent limitations on manuscript length and extent of graphic presentations.

- TECHNICAL MEMORANDUM. Scientific and technical findings that are preliminary or of specialized interest, e.g., quick release reports, working papers, and bibliographies that contain minimal annotation. Does not contain extensive analysis.

- CONTRACTOR REPORT. Scientific and technical findings by NASA-sponsored contractors and grantees.

- CONFERENCE PUBLICATION. Collected papers from scientific and technical conferences, symposia, seminars, or other meetings sponsored or cosponsored by NASA.

- SPECIAL PUBLICATION. Scientific, technical, or historical information from NASA programs, projects, and missions, often concerned with subjects having substantial public interest.

- TECHNICAL TRANSLATION. English-language translations of foreign scientific and technical material pertinent to NASA's mission.

Specialized services that complement the STI Program Office's diverse offerings include creating custom thesauri, building customized databases, organizing and publishing research results . . . even providing videos.

For more information about the NASA STI Program Office, see the following:

- Access the NASA STI Program Home Page at *http://www.sti.nasa.gov*

- E-mail your question via the Internet to help@sti.nasa.gov

- Fax your question to the NASA Access Help Desk at 301–621–0134

- Telephone the NASA Access Help Desk at 301–621–0390

- Write to:
  NASA Access Help Desk
  NASA Center for AeroSpace Information
  7121 Standard Drive
  Hanover, MD 21076

Foreign Object Damage in Disks of Two Gas-Turbine-Grade Silicon Nitrides by Steel Ball Projectiles at Ambient Temperature

Sung R. Choi
Ohio Aerospace Institute, Brook Park, Ohio

J. Michael Pereira, Lesley A. Janosik, and Ramakrishna T. Bhatt
Glenn Research Center, Cleveland, Ohio

National Aeronautics and
Space Administration

Glenn Research Center

Acknowledgments

This report is a formal draft or working paper, intended to solicit comments and ideas from a technical peer group.

Trade names or manufacturers' names are used in this report for identification only. This usage does not constitute an official endorsement, either expressed or implied, by the National Aeronautics and Space Administration.

The Propulsion and Power Program at NASA Glenn Research Center sponsored this work.

Foreign Object Damage in Disks of Two Gas-Turbine-Grade Silicon Nitrides by Steel Ball Projectiles at Ambient Temperature

Sung R. Choi
Ohio Aerospace Institute
Brook Park, Ohio 44142

J. Michael Pereira, Lesley A. Janosik, and Ramakrishna T. Bhatt
National Aeronautics and Space Administration
Glenn Research Center
Cleveland, Ohio 44135

Summary

Foreign object damage (FOD) behavior of two commercial gas-turbine-grade silicon nitrides, AS800 and SN282, was determined at ambient temperature through postimpact strength testing of disks impacted by steel ball projectiles with a diameter of 1.59 mm in a velocity range from 115 to 440 m/s. AS800 silicon nitride exhibited a greater FOD resistance than SN282, primarily due to its greater value of fracture toughness (K_{Ic}). The critical impact velocity V_c for which the corresponding postimpact strength was the lowest was $V_c \approx 440$ and 300 m/s for AS800 and SN282, respectively. A unique lower strength regime was typified for both silicon nitrides depending on impact velocity and was attributed to significant radial cracking. The damage generated by projectile impact was typically in the form of ring, radial, and cone cracks with their severity and combination being dependent on impact velocity. Unlike the thick (4 mm) flexure bar specimens used in our previous studies, the thin (2 mm) disk target specimens exhibited a unique back-side radial cracking on the reverse side just beneath the impact sites at and above impact velocities of 160 m/s for SN282 and 220 m/s AS800.

Introduction

Ceramics, because of their brittle nature, are susceptible to localized surface damage and/or cracking when subjected to impact by foreign objects. It is also true that ceramic components may fail structurally even from the impact of soft particles when their kinetic energy exceeds certain limits. The latter case has been often found in aerospace engines in which combustion products, metallic particles, or small foreign objects cause severe damage to blade/vane components, resulting in serious structural problems. Therefore, foreign object damage (FOD) associated with particle impact needs to be considered when ceramic materials are designed for structural applications. In view of this importance, a considerable amount of experimental and analytical work on impact damage of brittle materials by sharp particles as well as by blunt particles or plates has been accumulated (refs. 1 to 10). The understanding of particle impact phenomena has been based on the concept of indentation fracture mechanics for sharp particle impact (ref. 2) and on the Hertzian contact analysis for blunt or ball impact (ref. 1), leading to simplified quasi-static phenomenological models of strength degradation.

In our previous studies (refs. 11 and 12), FOD behavior of two representative gas-turbine-grade silicon nitrides, AS800 and SN282, was determined at ambient temperature using flexure bar test specimens. Rigidly supported ceramic target flexure specimens were impacted at their centers by steel ball projectiles with a diameter of 1.59 mm and velocities ranging from 220 to 440 m/s. Postimpact strength of the target specimens was determined as a function of impact velocity to accurately evaluate the severity of impact damage. AS800 silicon nitride exhibited a greater FOD resistance than SN282, due to its greater fracture toughness (K_{Ic}). The fact K_{Ic} was the key material parameter affecting FOD

resistance was further evidenced by the inferior FOD response of an additional equiaxed, fine-grained silicon nitride: this specimen possessed the lowest fracture toughness of the three silicon nitrides tested in these previous studies. The damage generated by projectile impact was typically in the form of well- or ill-developed ring or cone cracks with a limited occurrence of radial cracks.

The purpose of the present work, as an extension of the previous studies from references 11 and 12, was to investigate in great detail FOD behavior of AS800 and SN282 silicon nitrides at ambient temperature using a thin disk configuration of target specimens. The target disks were impacted at their centers at velocities ranging from 115 to 440 m/s by steel ball projectiles with a diameter of 1.59 mm. Postimpact strength of each disk specimen impacted was determined in ring-on-ring biaxial flexure as a function of impact velocity to evaluate the severity of impact damage. Fractography was performed before and after post impact strength testing to determine impact morphologies and the nature of strength-controlling flaw configurations. A static indentation experiment was also carried out to determine the relationship between indent load and impression size, which might be used to estimate impact force and impact energy.

A list of the symbols in this report is provided in the appendix.

Experimental Procedures

Materials and Test Specimens

Materials used in this work were the same as those used in our previous work, i.e., commercially available silicon nitrides AS800 (Honeywell, Torrance, CA, '99 vintage, gel-cast) and SN282 (Kyocera, Vancouver, WA, '00 vintage). These two silicon nitrides, both gas-pressure sintered, are currently considered as strong candidate materials for gas-turbine applications in view of their substantially improved elevated-temperature properties (refs. 13 to 15). Both materials are toughened silicon nitrides with microstructures tailored into elongated grain structures. The degree of elongation and the size of grains were greater in AS800 than SN282, as shown in figure 1. AS800 silicon nitride has been used at the NASA Glenn Research Center in life prediction programs (refs. 16 to 18); the present studies serve to increase the extensive knowledge base already established. The billets for each material were machined into disk test specimens measuring 2.0 by 45.0 mm, respectively, in thickness and diameter. The final finishing was completed with a #500 diamond grinding wheel under the specified conditions in accordance with ASTM standard C1161 (ref. 19). Prior to testing, all AS800 test specimens were annealed at 1200 °C in air for 2 h to eliminate or minimize damage and/or residual stresses presumably associated with machining. All SN282 test specimens were annealed by the manufacturer prior to testing with proprietary annealing condition.
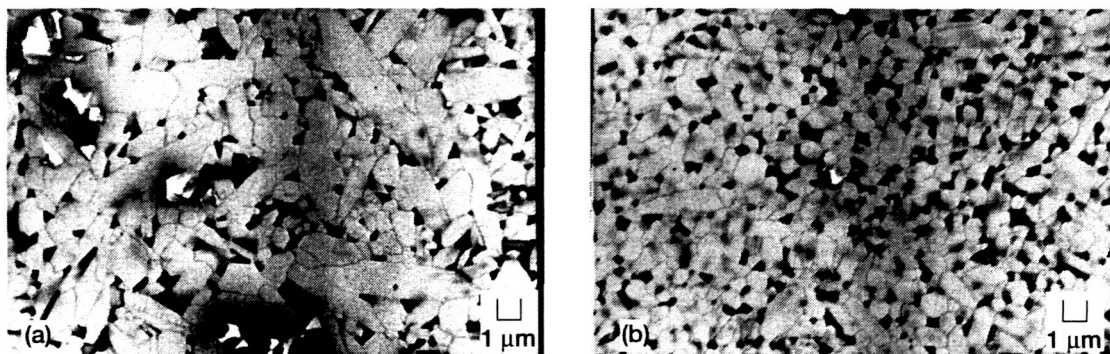

Figure 1.—Microstructures of silicon nitrides. (a) AS800. (b) SN282.

TABLE I.—BASIC MECHANICAL AND PHYSICAL PROPERTIES OF AS800 AND SN282 SILICON NITRIDES AND STEEL BALL PROJECTILES AT AMBIENT TEMPERATURE

[From ref. 12.]

Material	Elastic modulus,[a] E, GPa	Poisson's ratio,[a] ν	Density,[b] g/cm^3	Hardness,[c,f] GPa	Fracture strength[d]			Fracture toughness,[e,f] K_{Ic}, MPa m$^{1/2}$
					Mean strength,[f] MPa	Weibull modulus, m	Characteristic strength, MPa	
AS800 Si$_3$N$_4$	309	0.27	3.27	13.6(1.4)	775(45)	21	795	8.1(0.3)
SN282 Si$_3$N$_4$	304	0.28	3.32	15.3(0.2)	595(64)	11	623	5.5(0.2)
Chrome steel balls (SAE 52100)[g]	200	0.30	7.80	HRC ≥ 60	--------	--	---	--------

[a]By impulse excitation technique, ASTM C1259 (ref. 20).
[b]By mass/volume method.
[c]By Vickers microhardness indentation, ASTM C1327 (ref. 21).
[d]By four-point flexure with 20/40 mm spans, ASTM C1161 (ref. 19). Total of 20 test specimens used for each material.
[e]By single-edge-precracked-beam (SEPB) method, ASTM C 1421 (ref. 22). Total of five test specimens used for each material.
[f]Numbers in parentheses indicate ±1.0 standard deviation.
[g]Data from manufacturer; HRC is hardness in Rockwell C scale.

The basic mechanical and physical properties of AS800 and SN282 silicon nitrides as well as of the steel ball projectile material (SAE 52100 chrome steel) are shown in table I.

Foreign Object Damage Testing

The FOD testing was carried out at ambient temperature using the apparatus shown in figure 2. A detailed description of the apparatus can be found elsewhere (refs. 11 and 12). Hardened (HRC ≥ 60) chrome steel balls with a diameter of 1.59 mm were inserted into a 300-mm-long gun barrel with an inner diameter of 1.59 mm. A He-gas cylinder and relief valves were used to pressurize the reservoir to a specific level depending on prescribed impact velocity. Upon reaching a specific level of pressure, a solenoid valve was instantaneously opened accelerating a steel ball projectile through the gun barrel to impact a target specimen that was rigidly supported on an AS800 disk specimen (in 2-mm thickness and 45-mm diameter) backed on a rigid metallic specimen holder. Each target specimen was aligned such that the projectile impacted the center of the test specimen at an incidence angle normal to the surface.

For a given pressure, the velocity of each steel projectile was determined using two pairs of transmitter and receiver lasers, in which the two transmitters were aimed at the respective receivers through two holes in the gun barrel (see fig. 2). The distance between the two holes was 25 mm, with the front hole located about 70 mm away from the front end of the gun barrel. The time traveled by a projectile between the two holes was measured with a digital storage oscilloscope connected to the two pairs of transmitter and receiver lasers. The velocity was then calculated based on the distance-time relationship. A relationship between velocity and pressure was determined for a pressure range of 0 to 800 psi (ref. 12). It was found that velocity increased with increasing pressure, rising sharply at lower pressure but moderately at higher pressure. The impact velocity applied in this work ranged from 115 to 440 m/s. Typically, 10 test specimens were impacted at each chosen velocity for a given material. Impact morphologies at both impact site and back side of each impacted specimen were examined optically right after impact testing but prior to strength testing.
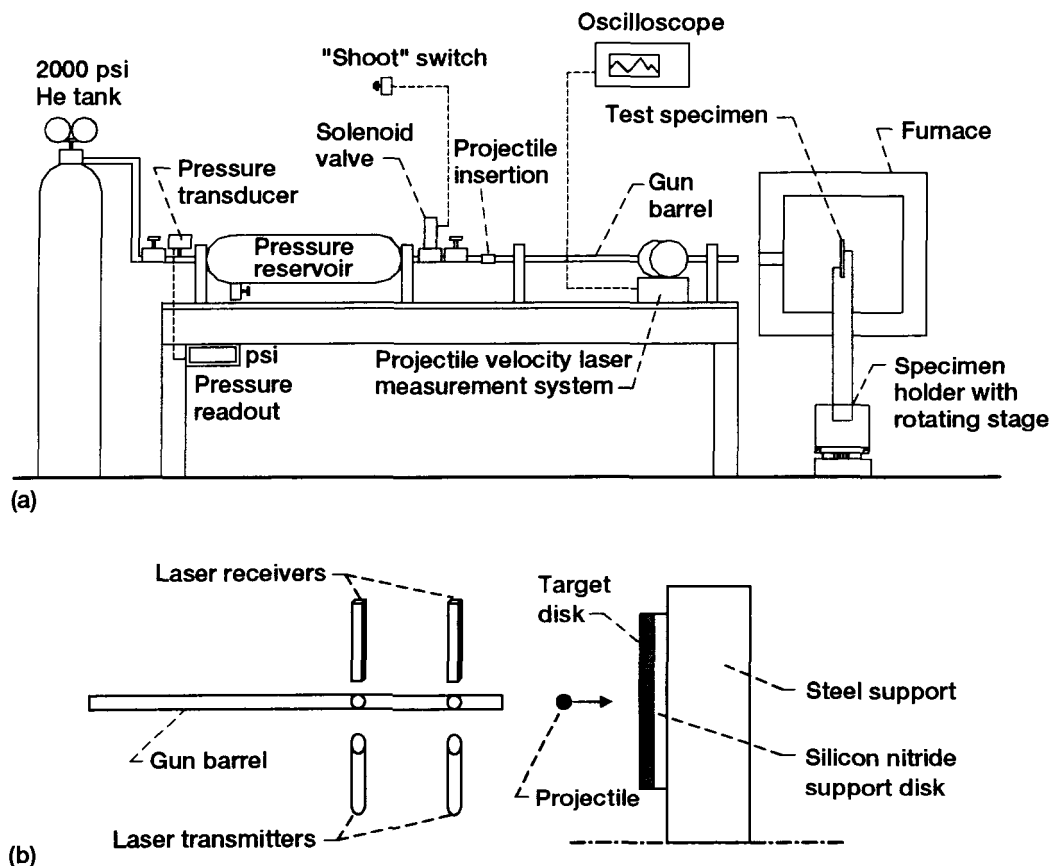
Figure 2.—Impact testing configuration. (a) Testing apparatus. (b) Detailed test arrangements.

Postimpact Strength Testing

Strength testing for impacted disks was performed in ambient-temperature air using a steel ring-on-ring biaxial flexure fixture with 20-mm load-ring and 40-mm support-ring diameters. A series of steel balls were used to eliminate frictional constraint at each of the load and support rings, similar to a thrust ball bearing assembly. Note that a continuous ring configuration, analogous to four-point flexure with fixed rollers, has exhibited fictional constraint as a source of stress error. Each impact-tested specimen was coaxially located in the biaxial flexure fixture such that its impact site was placed in tension. An electromechanical test frame (Model 8562, Instron, Canton, MA) was used for displacement control with an actuator speed of 0.5 mm/min. The slow crack growth that occurred during strength testing in air at ambient temperature for some ceramics such as alumina and glass-ceramics is not an issue for most silicon nitrides and silicon carbides. A fractographic analysis was performed after strength testing to determine failure origin, flaw configuration, mode of fracture and crack branching behavior. The as-received biaxial fracture strength was also determined for each material with 8 to 10 test specimens using the same test fixture, test frame, and test conditions that were utilized for the postimpact strength testing.

Static Indentation Testing

Static indentation testing was carried out for an AS800 disk specimen using the same ball projectiles employed in FOD testing. Each individual indentation load was applied (one at a time) with the respective ball indenter for about 20 s using a conventional twin-screw testing machine (Type TT, Instron, Canton,

MA). A total of eight indentation loads ranging from 0 to 292 N were used. The size (diameter) of contact marked in each ball indenter upon indentation, which was easily discernable as a flattened circle impression due to plastic deformation, was measured as a function of indentation load. An indentation load of 294 N was found to be the maximum applicable load beyond which the ball started to split, causing a total failure. The static indentation experiment was performed to determine a relationship between contact size and applied load with which a meaningful estimation and comparison could be made in terms of impact load and impression size actually involved in projectile impact.

Results and Discussion

Strength

As-received biaxial fracture strength.—The two-parameter Weibull plots of as-received biaxial fracture strengths of both AS800 and SN282 silicon nitrides are shown in figure 3, where $\ln\ln[1/(1-F)]$ was plotted as a function of $\ln\sigma_f$ with F and σ_f being failure probability and biaxial fracture strength, respectively. Note that the postimpact biaxial strengths of the specimens where failure was not initiated at the impact sites were included as as-received biaxial fracture strength data in the figure. The number of specimens used in the biaxial fracture strength data was 10 and 21, respectively, for AS800 and SN282. Weibull modulus m and characteristic strength σ_θ were $m = 18$ and $\sigma_\theta = 698$ MPa for AS800. For SN282, $m = 8$ and $\sigma_\theta = 451$ MPa. The mean strength was 678±45 MPa for AS800 and 426±60 MPa for SN282. The Weibull modulus for AS800 and SN282 ($m = 18$ and 8, respectively) in biaxial configuration compares well with the values determined previously ($m = 21$ and 11, respectively, see table I) for AS800 and SN282 in uniaxial four-point configuration (ref. 12), although the number of AS800 specimens (10) tested in the biaxial configuration might not be considered to be enough to give reliable Weibull parameters. Failure origins of both silicon nitrides, in many cases, were associated with surface-related defects such as machining flaws, pores, and elongated grains.
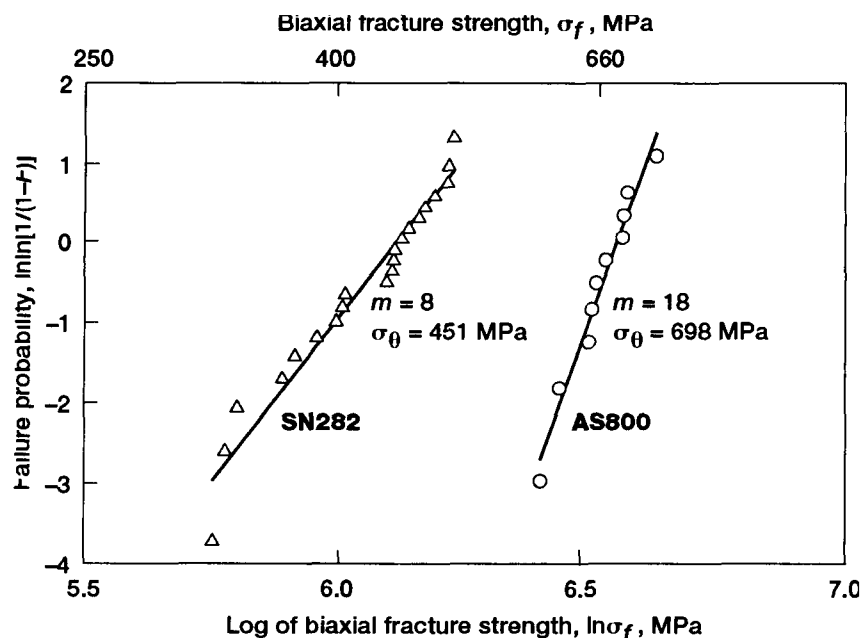

Figure 3.—Weibull distributions of biaxial strength of as-received AS800 and SN282 silicon nitride disks determined in ring-on-ring biaxial flexure at ambient temperature. Weibull modulus and characteristic strength are represented by m and σ_θ, respectively. Lines represent best fit.
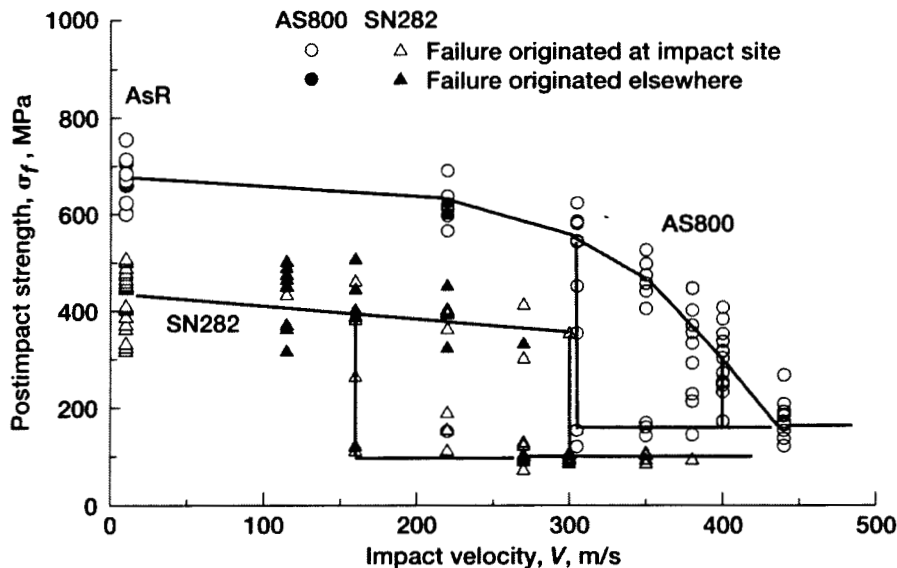
Figure 4.—Postimpact biaxial strength as function of impact velocity determined for AS800 and SN282 silicon nitride disks impacted by 1.59-mm-diameter steel ball projectiles at ambient temperature. "AsR" indicates as-received biaxial fracture strength of each material.

Postimpact strength.—The results of strength testing for impacted target specimens are shown in figure 4, where postimpact biaxial fracture strength was plotted as a function of impact velocity for both silicon nitrides. The biaxial fracture strength of both as-received materials was also included for comparison. Frequently, the specimens impacted at low velocities did not incur fractures originating from the impact sites and were indicated with closed symbols in the figure. For AS800, 2 specimens out of 10 did not obtain fractures originating from the impact sites when impacted at 220 m/s. For SN282, 1, 2, 4, and 9 (each out of 10) specimens did not fail from the impact at 270, 220, 160, and 115 m/s, respectively. Those specimens not failing from fractures initiating at the impact sites were equivalent in strength to the corresponding as-received specimens and thus were used to provide valid data in estimating the overall as-received biaxial fracture strength for each material.

As seen in the figure, the postimpact strength, in general, decreased with increasing impact velocity. Unlike the postimpact strength of flexure bars (refs. 11 and 12), the postimpact biaxial strength for a given impact velocity (greater than 220 and 160 m/s for AS800 and SN282, respectively) was typified with two distinct regions of strength: higher and lower strength regimes. The strength of the lower regime was around 150 and 100 MPa for AS800 and SN282, respectively. The lower strength regime started at 300 and 160 m/s for AS800 and SN282, respectively. The postimpact strength of each material converged to this lower regime strength as impact velocity sufficiently increased. This velocity at which a minimum (or the lowest) postimpact strength was retained is called the critical impact velocity (V_c) and was found to be the following:

$$V_c \approx 440 \text{ m/s for AS800}$$
$$V_c \approx 300 \text{ m/s for SN282}$$

These critical impact velocities for disks are in good agreement with those for flexure bars, for which $V_c = 400$ and 300 m/s were observed for AS800 and SN282, respectively (refs. 11 and 12). In the case of flexure bars, the test specimens failed upon impact at the critical impact velocity yielding a zero strength due to their small width (4 mm), whereas the disk specimens did not fracture upon impact but instead exhibited a significant size of radial cracks while retaining the lower regime strength in strength testing

because of their relatively large disk diameter (45 mm) compared to the size of the radial cracks. The details regarding impact morphologies and modes of fracture and other important features will be covered in the section **Impact Morphology and Fractography**.

Although not presented here, the two strength regimes were observed more clearly from Weibull plots. The unimodal strength distribution was characterized in as-received specimens at lower impact velocities, and at or above critical impact velocities, while the bimodality or trimodality was typified at intermediate impact velocities. A typical example of Weibull plots of both silicon nitrides at an impact velocity of 300 m/s is seen in figure 5. Nine out of ten SN282 specimens failed around the lower regime strength ($\approx$100 MPa) while AS800 failed more often at the higher strength regime, resulting in a bimodal or trimodal strength distribution.

An average value of postimpact strength at each of the higher and lower strength regimes was utilized to better represent the postimpact strength behavior for both silicon nitrides, and the results are depicted in figure 6. This figure clearly shows features such as the two strength regimes, the strength envelope between the related impact velocities, and the critical impact velocity, etc. From these results as well as from figure 4, it can be concluded that resistance to FOD is greater in AS800 than in SN282, consistent with the previous FOD results on flexure bar specimens at ambient temperature (refs. 11 and 12).

Impact Morphology and Fractography

Steel ball projectiles.—Some of the steel ball projectiles were collected after impact for fractographic analysis. The hardened steel ball projectiles were flattened after impact from plastic deformation. In some cases, the projectiles were subjected to both extreme heat—evidenced by burning marks—and cracking, particularly at higher impact velocity. The degree of plastic deformation of the projectiles in terms of their decrease in diameter was about 20 to 40 percent depending on impact velocity. Also note that the flattened surfaces of the steel ball projectiles retained the impression of the machining marks of ceramic
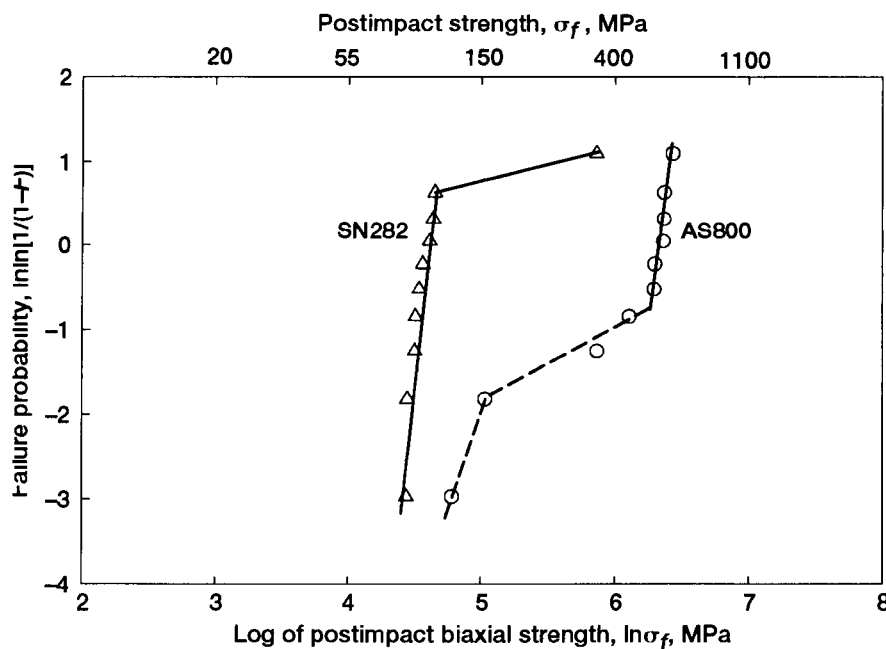

Figure 5.—Weibull postimpact biaxial strength distributions for AS800 and SN282 silicon nitride disks impacted at 300 m/s by 1.59-mm-diameter steel ball projectiles at ambient temperature.
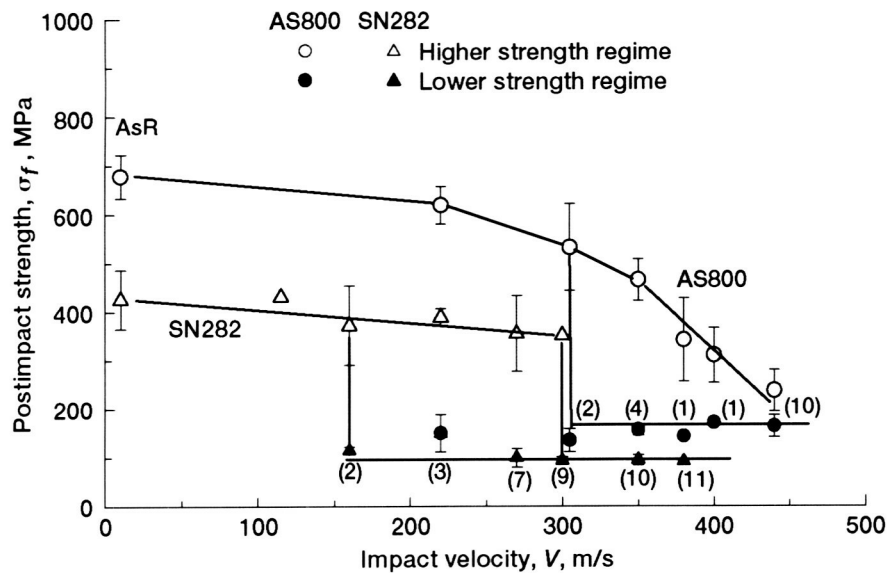
Figure 6.—Mean postimpact biaxial strength as function of impact velocity for AS800 and SN282 silicon nitride disks impacted by 1.59-mm-diameter steel ball projectiles at ambient temperature. Error bars indicate ±1.0 standard deviation. "AsR" indicates as-received biaxial fracture strength of each material. Numbers in the parentheses represent number of test specimens that failed at the lower strength regime.
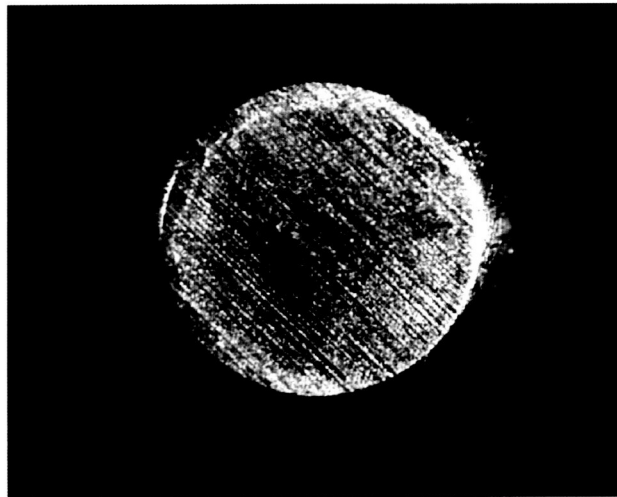

Figure 7.—Steel ball projectile after impact at velocity of 220 m/s on AS800 silicon nitride target. Note impressions from machining marks of AS800 specimen.

target specimens with a series of numerous parallel lines, indicative of the significant severity of impact involved, shown in figure 7.

Target specimens.—The following sections describe the features found on the target specimens resulting from impact.

Impression marks: The impression marks, generated because of material transfer upon impact from steel ball projectiles to ceramic target specimens in a phenomenon known as a cold welding, exhibited a unique feature such that they were in the form of rings, having inner and outer diameters, as seen in
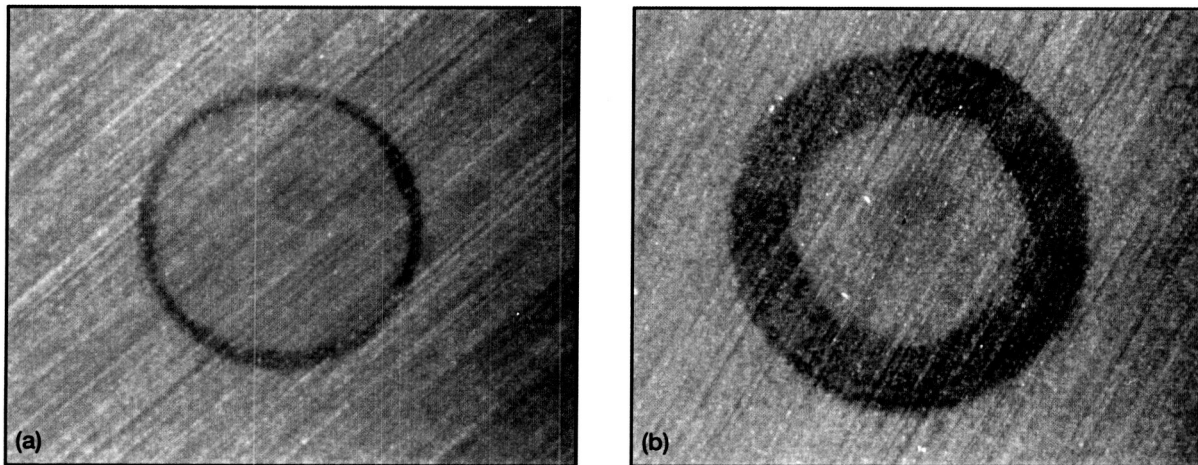
Figure 8.—Typical impression marks on AS800 silicon nitride disks showing ring shape from impact by 1.59-mm-diameter steel ball projectiles at (a) 220 and (b) 350 m/s.
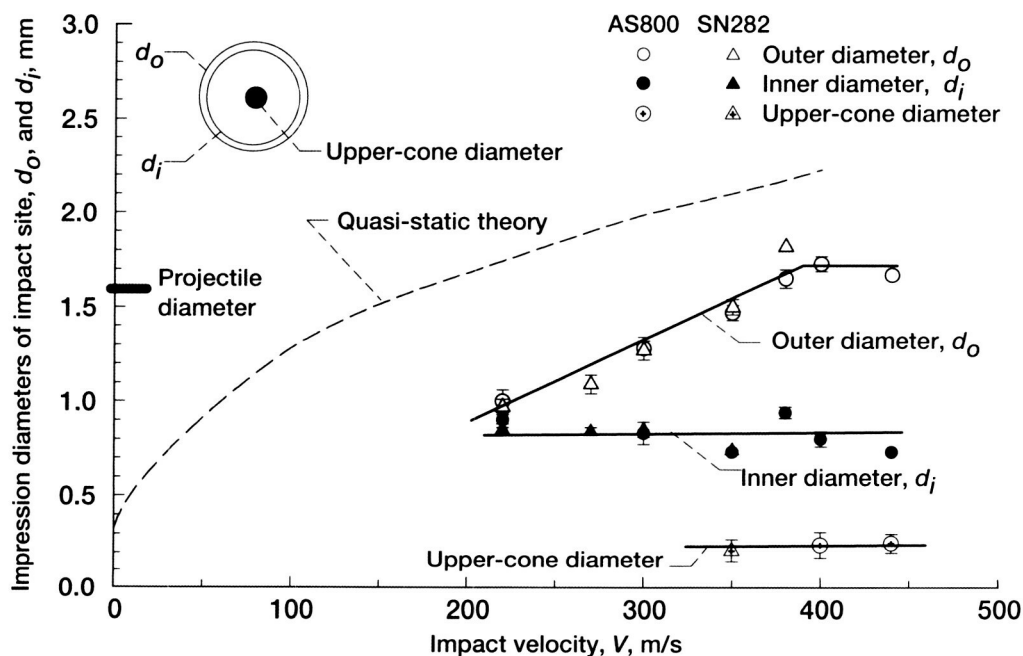

Figure 9.—Impression size generated on impact sites of target specimens as function of impact velocity for AS800 and SN282 silicon nitride disks impacted by 1.59-mm-diameter steel ball projectiles at ambient temperature. The contact-area diameter estimated by the quasi-static contact theory (2a, eq. (2)) is included for comparison. Upper-cone size data are also shown.

figure 8. The sizes of inner and outer diameters were measured optically for the specimens impacted at and above 220 m/s. The impression marks were either not visible or not produced on the specimens impacted below 220 m/s (applied to SN282), attributed to insufficient impact force to cause cold welding. At higher impact velocities of 400 to 440 m/s for AS800, significant material transfer was observed with a sign of outward splashing of metal. The measurements of the impression marks for both silicon nitrides are shown in figure 9. The measurements were made using a total of 5 to 10 specimens at each impact velocity. The outer diameter d_o increased with increasing impact velocity for both silicon nitrides, approaching approximately the diameter of projectile; whereas the inner diameter remained almost

constant with an average of d_i = 0.82±0.07 mm, regardless of impact velocity. Also note that the size of impression was independent of material because the basic properties (elastic modulus, Poisson's ratio, hardness, and density, etc.) of the two silicon nitrides, which control Hertzian contact phenomenon, are basically identical. It is natural to consider that the outer diameter of impression would correspond to the outside diameter of ball projectile upon impact and that it would increase with increasing impact velocity. However, the unchanging nature of inner diameter with increasing impact velocity as well as the occurrence of ring shape on impact sites imposes a difficulty in understanding the details of the deformation mechanism(s) involved therein.

The tensile principal stress, according to the Hertzian contact analysis, occurs just outside the area of contact between two contacting bodies in which a cone crack initiates and propagates through the locus of maximum tensile stress (refs. 5 and 9). In cases of impacts with hard projectiles and hard target materials (such as ceramic balls and ceramic target materials), it has been shown that agreement between the calculated contact area (radius) and the upper size (radius) of a cone was reasonable (ref. 4). The contact area can be estimated based on the Hertzian contact theory together with the principle of conservation of impact energy as follows (refs. 1, 4, 5, and 8):

$$a = \alpha\left(\frac{k}{E}\right)^{\frac{1}{5}} \rho^{\frac{1}{5}} R V^{\frac{2}{5}} \tag{1}$$

where a is the radius of contact area, α is a constant ($\approx$1.3), E is the elastic modulus of the target material, ρ is the density of the projectile, R is the radius of projectile, and V is the impact velocity. The parameter k is expressed as

$$k = \left(1 - v^2\right) + \left(1 - v'^2\right)\frac{E}{E'} \tag{2}$$

with v being Poisson's ratio and the primes denoting variables associated with the projectile. As shown in figure 9, the calculated contact area $2a$ based on equation (2) was significantly greater than the impression sizes observed. However, it should be noted that a direct comparison should not be made between the calculated and the observed values since the calculated impression size was unrealistically large, indicating that the calculated values were in the range of significant plastic deformation. As a consequence, the impact events in this work can be characterized as plastic (in projectile)-elastic (in target material) rather than elastic-elastic impact that is the case for ceramic balls versus ceramic target. It is interesting to note from the figure that a consistent size (0.23-mm diameter) of upper cone was observed regardless of impact velocity. This phenomenon contradicts the Hertzian theory, which states that the contact area increases with increasing impact velocity and that the tensile principal stress occurs just outside contact area, in which a cone crack initiates and propagates through the locus of maximum tensile stress (refs. 5 and 9). The discrepancy is believed again to be due to the significant plastic deformation, which may make Hertzian contact theory inapplicable.

Fracture surfaces: At lower impact velocities, both AS800 and SN282 specimens failed similarly from ring cracks, in which a part of the ring contour was seen at failure origin as a small curved portion. The fracture surfaces also pertained such a curved portion, as seen in figure 10. At intermediate impact velocities for each material, both ring and radial cracks were associated with failure. The upper cones located at the impact center, whether somewhat well developed or not, seemed to be rarely associated with failure origins. Figure 11 shows failure location as a function of postimpact strength determined for the specimens failing from ring cracks, which typically impart medium to high strengths at low to intermediate impact velocities. An average value of failure location measured from the impact center was 0.28±0.07 mm (or 0.56-mm diameter). This indicates that the strength-controlling ring cracks were situated between the inner diameter (0.82 mm) of impression and the outside of the upper cone diameter (0.23 mm). The lower strength regime, typified at intermediate velocities of each material, was associated
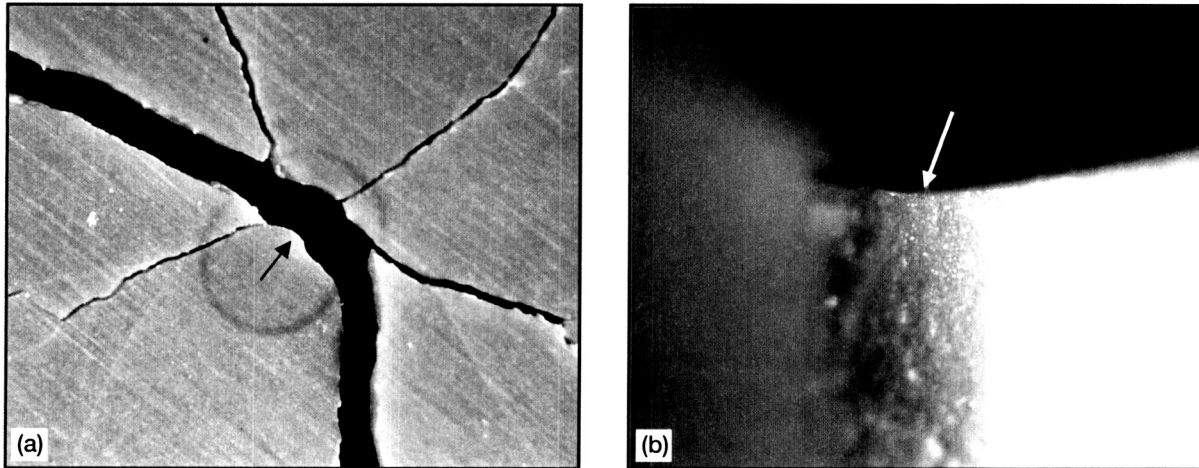
Figure 10.—Example of AS800 silicon nitride disk that failed from ring crack in postimpact strength testing. Specimen was impacted at low velocity of 220 m/s by 1.59-mm-diameter steel ball projectile. (a) Impact site. (b) Corresponding fracture surface, with arrows indicating failure origin. Corresponding postimpact strength was 616 MPa.
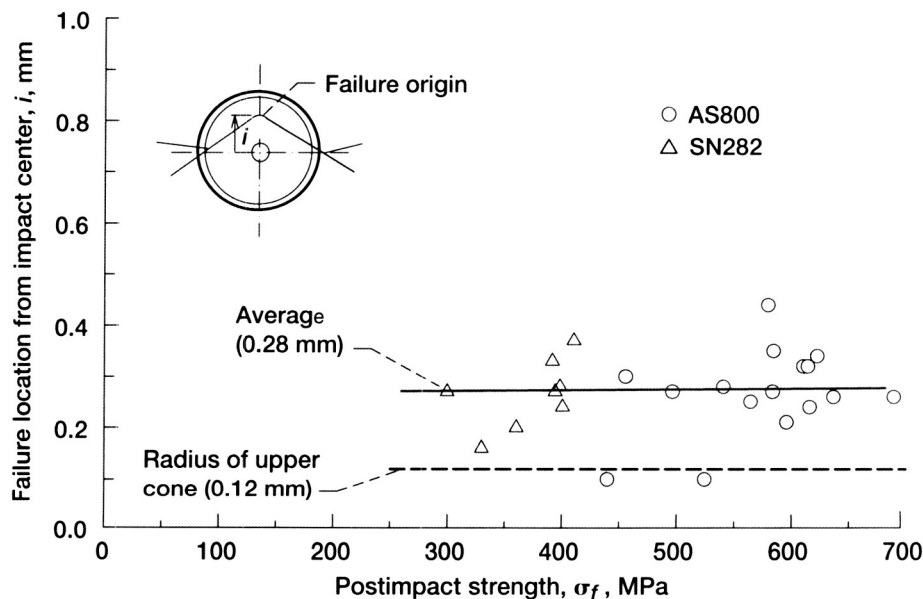

Figure 11.—Failure location distance from impact center as function of postimpact strength for silicon nitride disks that failed from ring cracks, which impart overall medium to high postimpact strength. Average radius of upper cone is also indicated as dashed straight line for comparison.

exclusively with well-developed radial cracks ranging in size from 3 to 5 mm, emanating from the impact sites, as shown in figure 12. These well-developed radial cracks resulted in the lower strength regime around 150 and 100 MPa, respectively, for AS800 and SN282. Hence, it is important to note that the existence of lower strength regime was due to the occurrence of these significant radial cracks.

At higher impact velocities close to or above the critical impact velocity, failure of both materials was mainly associated with well-developed radial cracks even though well-developed cone cracking invariably occurred simultaneously. In many cases, cones with lower diameters ranging from 4 to 6 mm
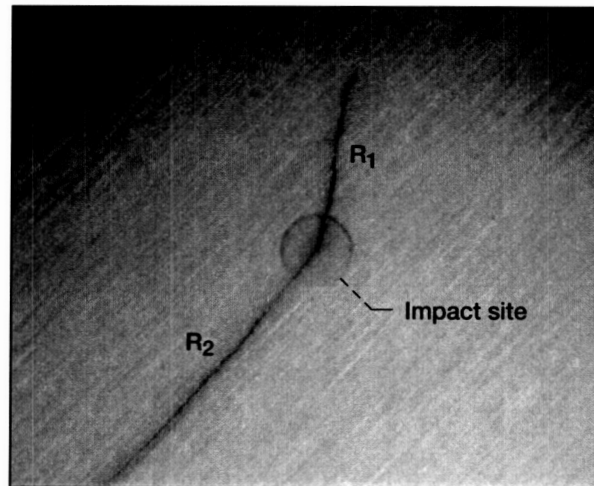
Figure 12.—Example showing significant radial cracks (R_1 and R_2) in AS800 silicon nitride disk impacted at 220 m/s by 1.59-mm-diameter steel ball projectile. Resulting postimpact strength of this specimen, controlled by the 4.7-mm crack R_2, was 151 MPa.

were separated from the specimen after strength testing. A typical impact site showing the impression, radial cracks, and an upper cone together with a back-side view (this will be discussed later in the section **Consideration of Back-Side Cracking**), a fracture surface, and a separated cone is shown in figure 13. The dimensions of the cones, including upper and lower diameters and heights, were determined for both silicon nitrides from either fracture surfaces or separated cones using typically seven specimens in measurements at each impact velocity. The cone angle, defined as half of apex angle, was calculated based on the determined cone geometry.[1] The result is shown in figure 14. The cone angle with an average value of $42\pm2°$ remained almost unchanged regardless of material over impact velocities from 350 to 440 m/s. There is limited information in the literature on cone angles resulting from impact of a ceramic target by steel ball projectiles, and it is available only as photographs (e.g., ref. 23), so a meaningful comparison between this work and the published data could not be made. However, it should be noted that the angle also depends on variables such as specimen geometry, type of specimen support, projectile material, and impact velocity.

In the simultaneous presence of ring, radial, and cone cracks, the radial cracks were the most influential in controlling the magnitude of postimpact strength. Hence, it is important to scrutinize in more detail the occurrence and sizes of radial crack as a function of impact velocity for a given material. Figure 15 shows the probability of occurrence of radial cracks as a function of impact velocity. For a given impact velocity, the occurrence of radial cracking was greater in SN282 than in AS800, attributed to lower fracture toughness in SN252 (see table I). The figure also indicates that the critical impact velocity, 300 and 440 m/s for SN282 and AS800, respectively, corresponds to the case where the probability of occurrence is close to 100 percent for each material. Plots of postimpact strength versus radial crack sizes are shown in figure 16. The solid line for each material indicates a prediction of strength based on the semicircular crack assumption, $\sigma_f = K_{Ic}/[Y(c_f)^{1/2}]$, where $Y = \sqrt{\pi}/2$ is the crack geometry factor, and c_f is the crack length at fracture. It was observed that in many cases radial cracks were semi-elliptical and irregular (not straight or symmetric) in their shapes. Notwithstanding, the semicircular

---

[1]Strictly speaking, the cones were not straight but a little curved particularly toward their bottom. The calculation of cone angle, however, was made based on the straight line extended to the bottom in some cases.
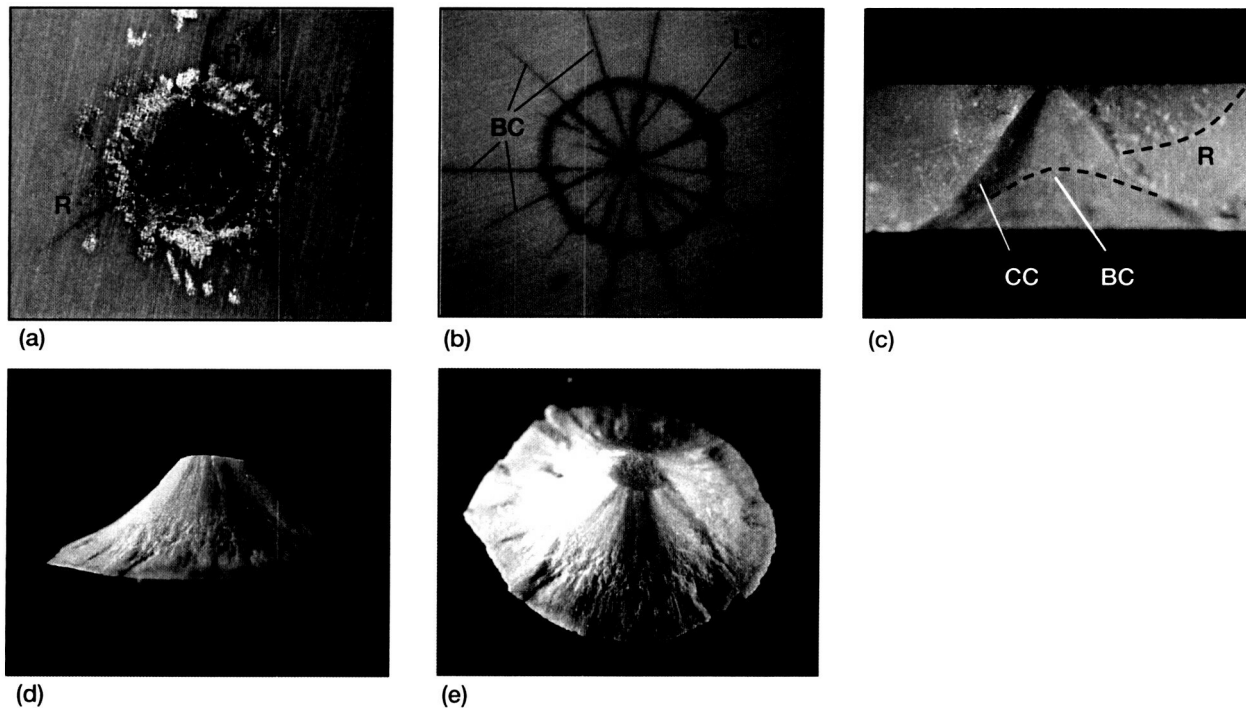
Figure 13.—Examples of impact damage occurring in AS800 silicon nitride disk impacted at high velocity of 44 m/s by 1.59-mm-diameter steel ball projectile. (a) Impact site showing impression, radial cracks (R), and upper cone (UP) before strength testing. (b) Back-side view showing back-side radial cracks (BC, radiating from center) and lower diameter of a cone (LC) before strength testing. (c) Fracture surface showing cavity of cone (CC), impact-site (upper) radial cracks (R), and back-side radial cracks (BC). (d) Side view of cone separated from (c). (e) Top view of cone separated from (c). Corresponding postimpact strength of target specimen was 192 MPa.
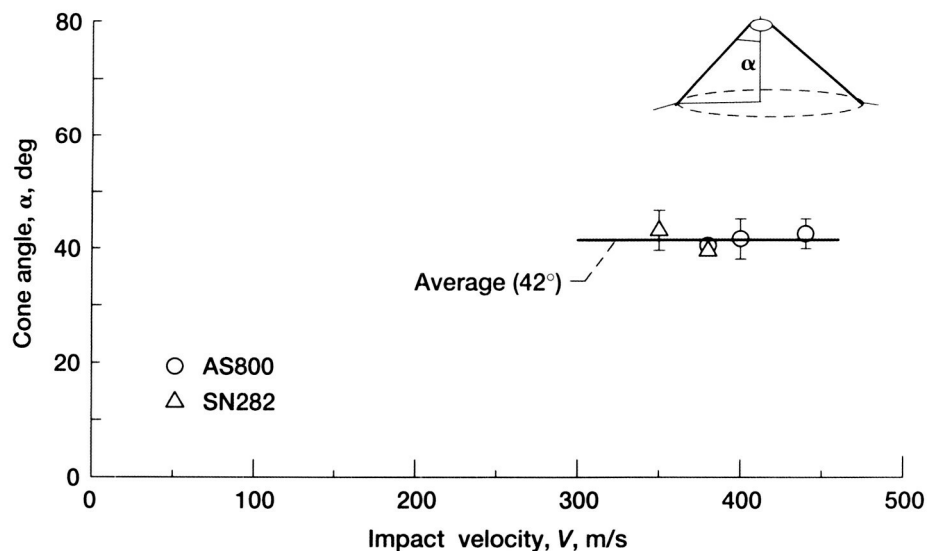

Figure 14.—Cone angle as function of impact velocity for AS800 and SN282 silicon nitride disks impacted by 1.59-mm-diameter steel ball projectiles at ambient temperature. Note that cones developed mainly at higher impact velocities. Error bars indicate ±1.0 standard deviation.
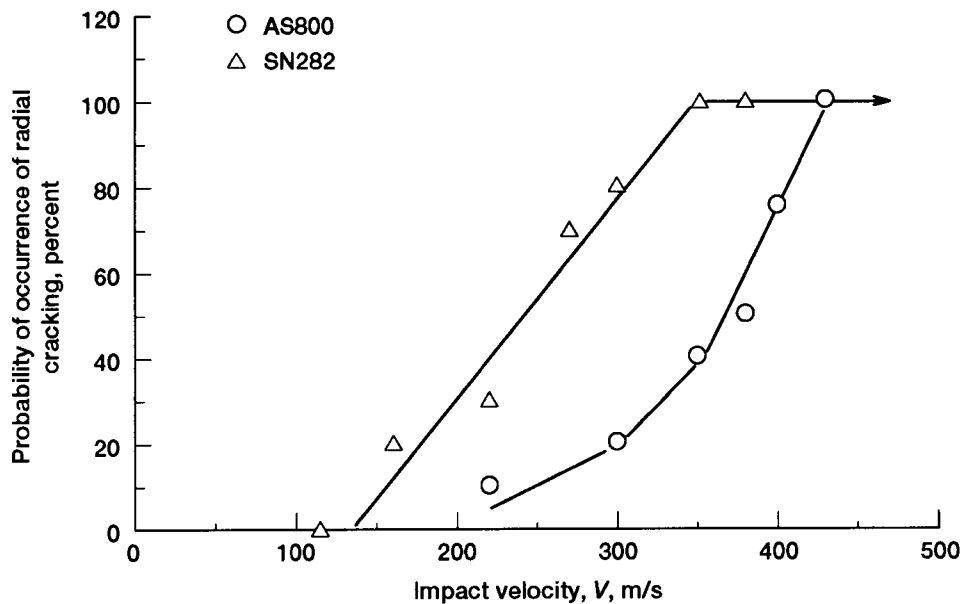
Figure 15.—Probability of occurrence of radial cracking as function of impact velocity for AS800 and SN282 silicon nitride disks impacted by 1.59-mm-diameter steel ball projectiles at ambient temperature.
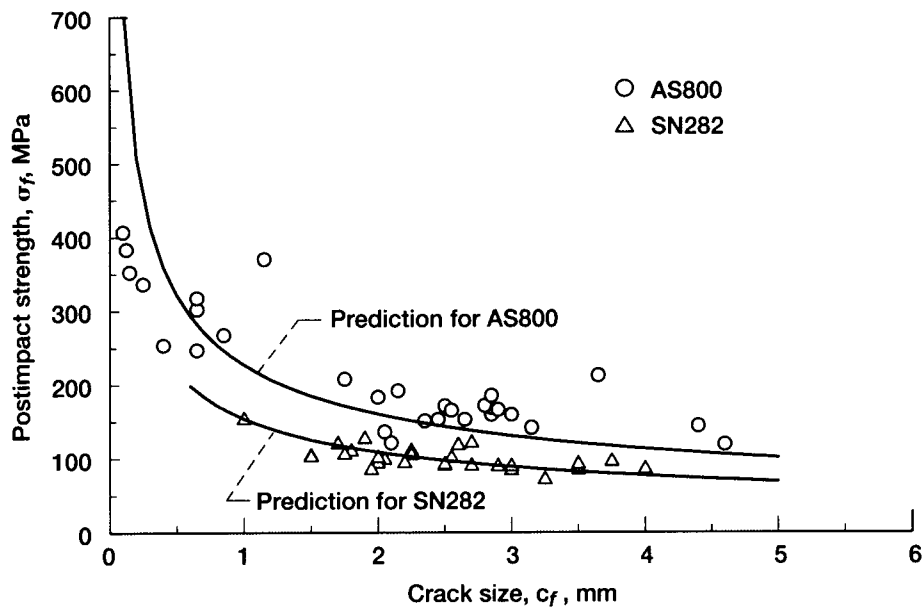

Figure 16.—Postimpact strength as function of radial crack size for AS800 and SN282 silicon nitride disks impacted by 1.59-mm-steel ball projectiles at ambient temperature. Solid lines represent predictions based on semi-circular crack assumption.

prediction is in good agreement with the experimental data, possibly eliminating or minimizing the need for experimental data to determine the postimpact strength.

Back-side cracking: Unlike flexure bar specimens, disk target specimens exhibited a peculiar feature of back-side cracking that occurred on the reverse side of disks depending on impact velocity. Typical back-side cracking generated upon impact—but prior to postimpact strength testing—and the corresponding fracture surface are shown in figure 17. Well-defined and somewhat symmetric radial cracks originated in the reverse side of the specimen from a point just beneath the impact site. The crack configuration was semi-elliptical with a minor to major axis ratio of around 0.2 to 0.3. The occurrence of back-side cracking increased with higher impact velocity, as shown in figure 18(a). For a given impact velocity, the probability of occurrence of back-side cracking was a little greater in SN282 than in AS800, again due to lower fracture toughness in SN282 than in AS800. The sizes of back-side cracks, measured from its center, are shown in figure 18(b). AS800 showed almost consistent crack size independent of impact velocity with a mean size of around 6 mm, whereas SN282 showed a dependency of crack size on impact velocity such that the crack size increased with impact velocity. The reason for the occurrence of back-side cracking in disk target specimens, very important in view of potential structural integrity, will be discussed later in the section **Consideration of Back-Side Cracking**.

Crack branching: A typical crack branching pattern of a target specimen in strength testing is shown in figure 19, as also inferred from figure 10(a). The empirical relation between biaxial fracture strength σ_f (in MPa) and crack branching length has been shown as (e.g., ref. 24)

$$\sigma_f r_b^{1/2} = A_b \tag{3}$$

where r_b is the crack branching length in meters, assumed to be straight, and A_b is the branching constant in $MPa\,m^{1/2}$. Figure 20 shows the results of postimpact strength as a function of crack branching length determined for both silicon nitrides. A good correlation between strength and branching length was observed in SN282 with a branching constant of $A_b = 8.7\pm1.0$ $MPa\,m^{1/2}$. By contrast, AS800 did not exhibit a reasonable correlation because of significant scatter. The crack branching constant for AS800 was $A_b = 12.6\pm4.2$ $MPa\,m^{1/2}$. This branching constant, however, is in reasonable agreement with the branching constant ($A_b = 14.9\pm1.9$ $MPa\,m^{1/2}$) of the same material ('99 vintage) determined previously in uniaxial flexure (20/40 mm spans, ASTM B type specimens) (Choi, S.R.: Fracture Mirror Constant Versus Fracture Toughness for Various Advanced Structural Ceramics. Presented at the American Ceramic Society Annual Meeting, April 28, 2002, St. Louis, MO.). The ratio of crack branching constant to fracture toughness was $A_b/K_{Ic}=1.56$ and 1.58, respectively, for AS800 and SN282. Although 3 has long
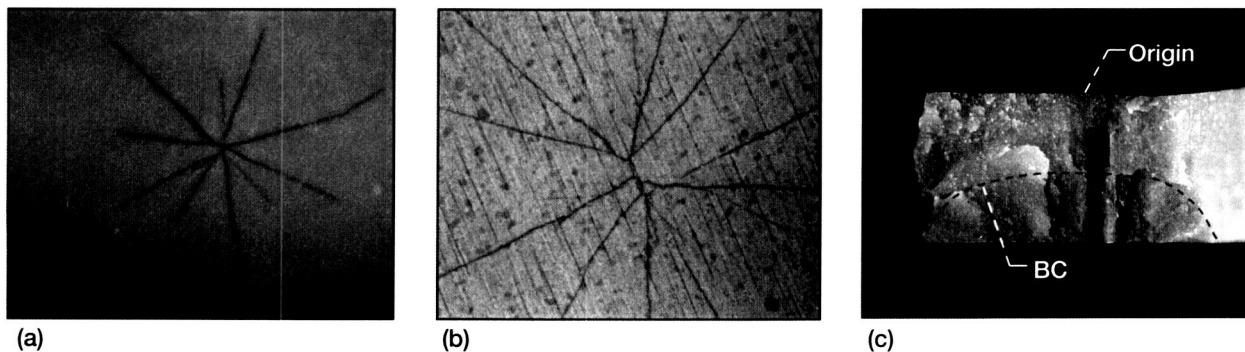

(a)   (b)   (c)

Figure 17.—Examples of well-developed back-side radial cracking and fracture surface. (a) AS800 silicon nitride disk impacted at 300 m/s (before strength testing); corresponding postimpact strength, 450 MPa. (b) SN282 silicon nitride disk impacted at 300 m/s (before strength testing); corresponding postimpact strength, 96 MPa. (c) Fracture surface of AS800 specimen in (a) showing back-side cracks (BC) and failure origin.
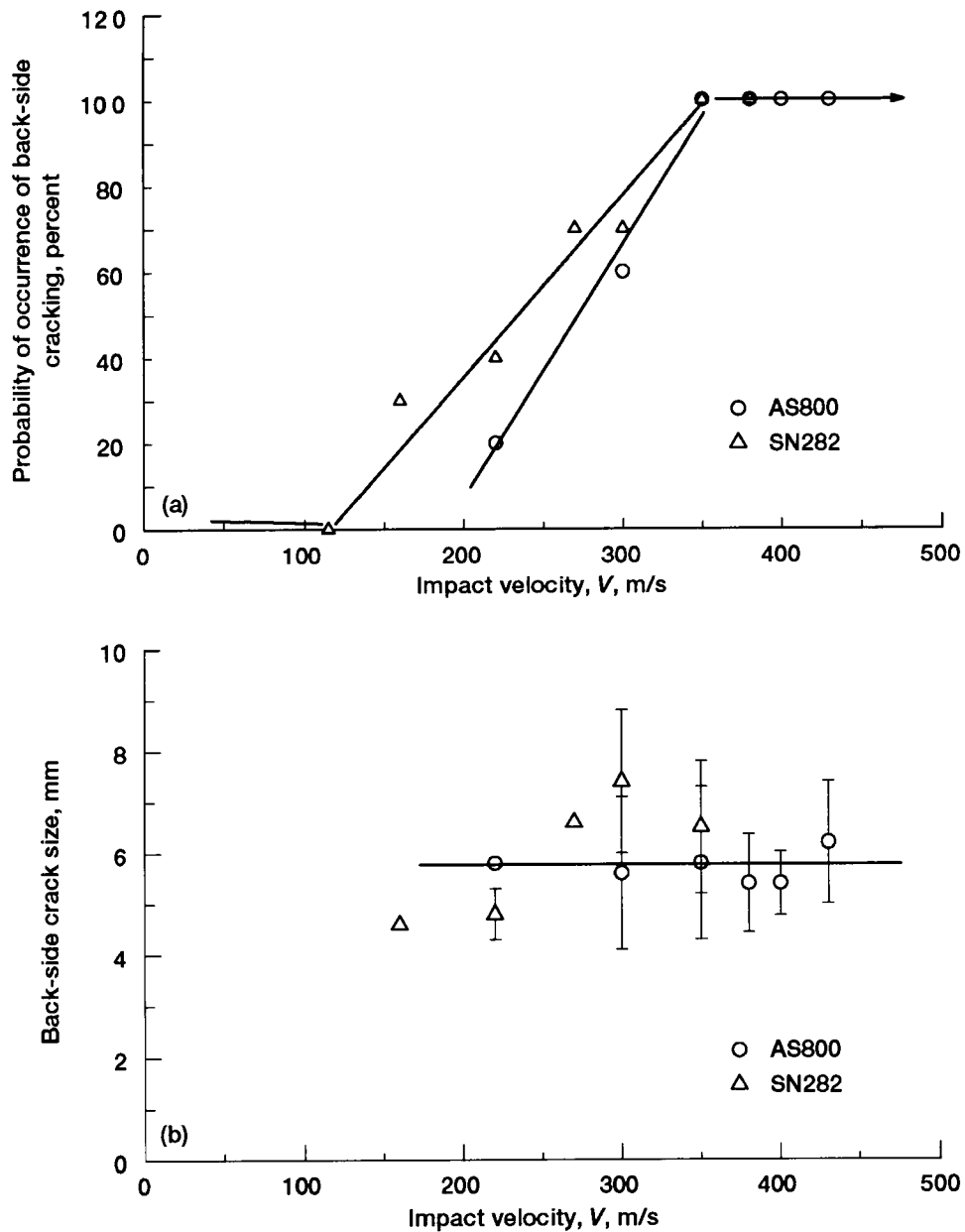
Figure 18.—AS800 and SN282 silicon nitride disks impacted at different velocities by 1.59-mm-diameter steel ball projectiles at ambient temperature. (a) Probability of occurrence of back-side cracking. (b) Size of back-side cracks. Error bars indicate ±1.0 standard deviation.
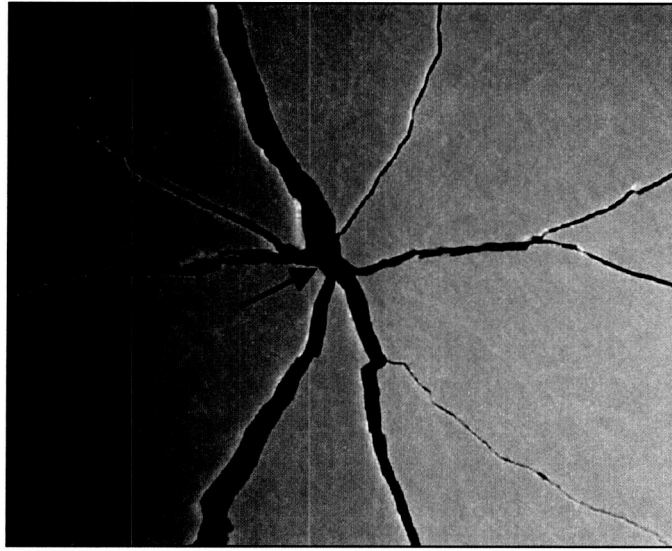
Figure 19.—Typical pattern of crack branching for AS800 silicon nitride disk impacted by 1.59-mm-diameter steel ball projectile. Arrow indicates failure origin.
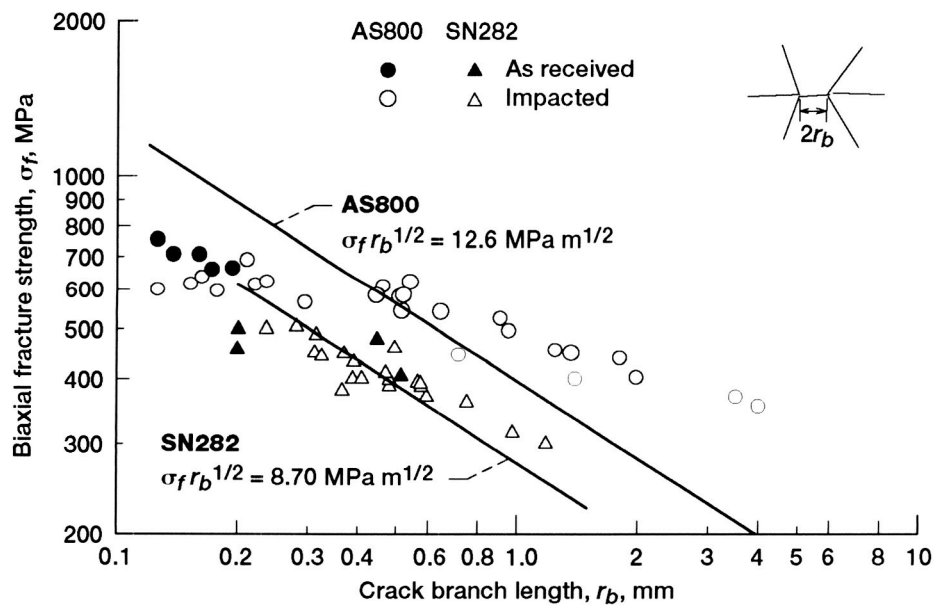

Figure 20.—Biaxial strength as function of crack branch length for as-received and impacted disks of AS800 and SN282 silicon nitrides at ambient temperature. Solid lines represent best-fit lines based on equation (4).

been regarded as the value of A_b/K_{1c} for brittle materials and ceramics (e.g., ref. 24), a recent study on the fracture branching constant for various advanced ceramics (ref. 25) has shown that the value is actually closer to 2. Hence, the determined A_b/K_{1c} ratio for both AS800 and SN282 in biaxial flexure is said to be within the range generally found in many recent advanced ceramics.

Static Indentation

Experimental results.—The static indentation experiments with projectile ball indenters on an AS800 silicon nitride disk showed that a flattened circular area of contact—a sign of significant plastic deformation—was well developed on each ball indenter, and as expected its size (or diameter) depended on applied indent load. There was no visible sign of damage in contact area in the AS800 disk. The experimental results are shown in figure 21 where contact diameter d was plotted against applied static indent load P_s. The best-fit line was represented as follows:

$$d = 0.01277 P_s^{1/2} \tag{4}$$

The average compressive contact pressure cp calculated from the slope of the best-fit line based on a relationship of $cp = 4P_s/(\pi d^2)$ was found to be 7815 ± 1063 MPa (with a coefficient of variation of 13.6 percent) in the range of indent loads applied from 0 to 2943 N. This contact pressure was surprisingly consistent regardless of indent load, indicating that the plastic flow stress occurring in the steel ball projectile upon indent loading is almost constant. Because of the negligible elastic strain compared with plastic strain involved, it could be reasonable to take the average contact pressure as compressive plastic flow stress of the ball projectile; thus it could be possible to use a rigid-perfectly plastic assumption. Therefore, the plastic flow stress of the ball projectile in compression, σ_p, is
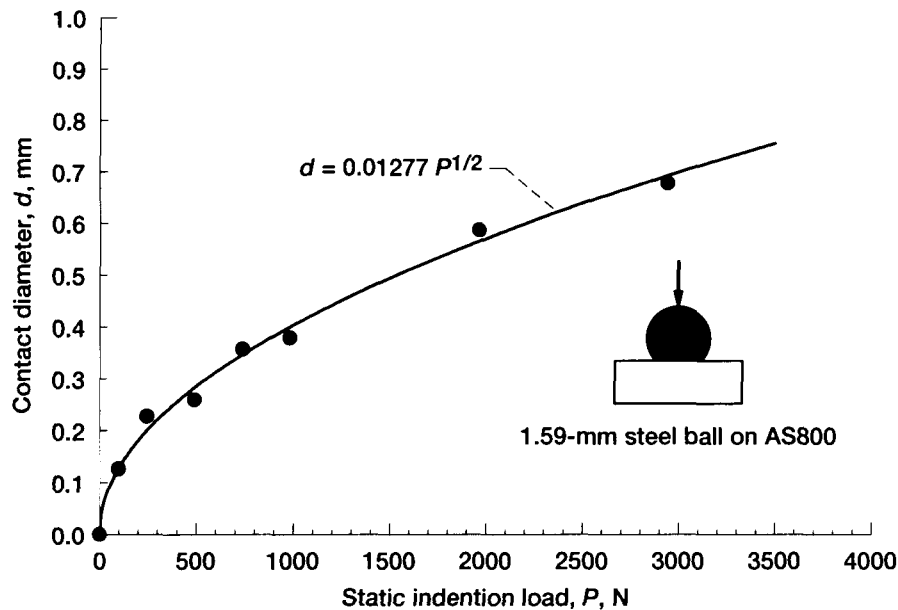
$$\sigma_p = 7815 \text{ MPa}$$

Figure 21.—Contact diameter as function of static indentation load determined with AS800 silicon nitride disk and 1.59-mm-diameter steel ball indenter. Line represents best fit.

Assuming this compressive plastic flow stress was operative even in impact event, the maximum impact force as well as impact kinetic energy will be estimated below.

Estimation of quasi-static impact force.—The size of contact area produced in the target disks upon impact was determined as a function of impact velocity, as already seen in figure 9. Taking the outside diameter d_o of impact impression as representative contact size (assuming full contact with a size of outside diameter) and using the compressive plastic flow stress determined above, impact force P was quasi-statically estimated for a given impact velocity using the following relation

$$P = \sigma_p A \tag{5}$$

where A is the contact area $(\pi d_o^2 / 4)$ that can be calculated for a given impact velocity with the value of d_o taken from the results of figure 9. The results of impact force estimations are shown in figure 22 for both AS800 and SN282 silicon nitrides. The figure also includes the estimation by the frequently quoted, quasi-static contact theory (refs. 1, 4, 5, and 8) that is based on the principle of energy conservation:

$$P = \alpha \left(\frac{k}{E}\right)^{-2/5} \rho^{3/5} R^2 V^{6/5} \tag{6}$$

The quasi-static contact theory predicted the impact force 50 to 100 percent greater than the static indentation approach based on plasticity. Although it is unknown as to which approach would yield a better estimation, it is manifest that the quasi-static contact theory, which assumed the impact event as an idealized elastic (in projectile)-elastic (target) phenomenon, would overestimate the impact force. Although the discrepancy is significant between the two approaches, the result shown in the figure gives an insight regarding the magnitude of impact force, even reaching two to three metric tons (!) at a high impact velocity of 400 m/s. Note that appropriate instrumentation should be utilized to better describe the evolution and magnitude of force during the impact.
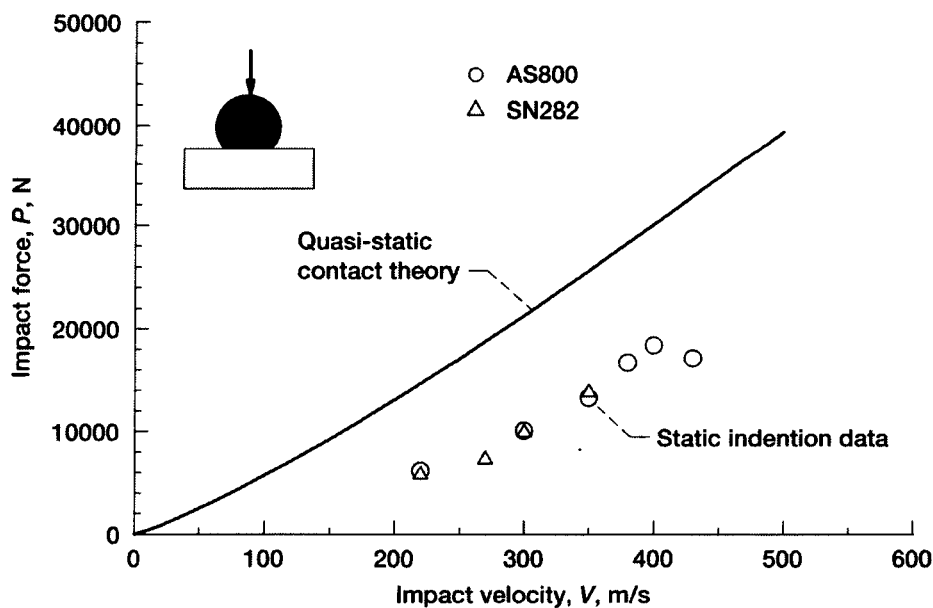

Figure 22.—Impact force as function of impact velocity estimated from results of static indentation experiments. Impact force evaluated by quasi-static contact theory, equation (8), is also included for comparison.

Estimation of quasi-static impact kinetic energy.—The kinetic energy of impacting ball projectile U_K is customarily defined as

$$U_K = \frac{1}{2} m_p V^2 \tag{7}$$

where m_p is the mass of ball projectile. Assuming that the ball projectile behaves rigidly-perfectly plastic based on the result of the static indentation experiments and that the impact kinetic energy is all consumed in the plastic deformation of ball projectile, the energy associated with plastic deformation of ball projectile can be estimated using the flowing relation:

$$U_{KP} = \int \sigma_p A \, dz$$
$$= \pi \sigma_p z^2 \left(R - \frac{z}{3} \right) \tag{8}$$

where z is the deformation (or impression) depth of ball projectile (see fig. 23) that can be calculated easily with the determined impression size (d_o) from

$$z = \frac{1}{2} \left[2R - \left(4R^2 - d_o \right)^{\frac{1}{2}} \right] \quad \text{for } d_o \leq 2R \tag{9}$$

U_{KP} was calculated using equation (10) with d_o determined (fig. 9) for a given impact velocity. The resulting plots of kinetic energy evaluated with both U_K and U_{KP} are shown in figure 23. The discrepancy between the two approaches was small at lower impact velocity but was amplified with increasing impact velocity ($V \geq 300$ m/s). The discrepancy occurring at higher impact velocity could be due to the volume
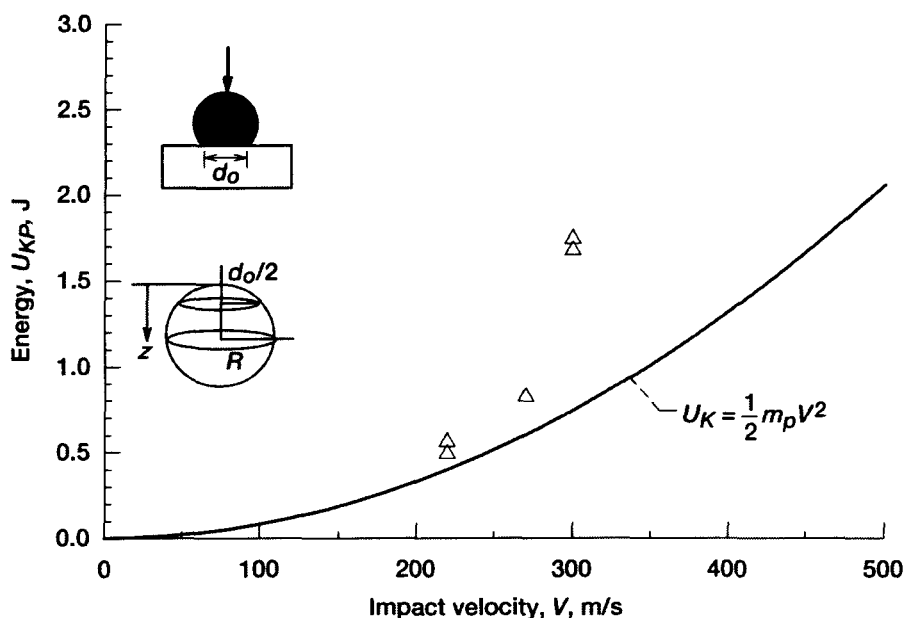

Figure 23.—Impact kinetic energy U_{KP} as function of impact velocity V estimated with equation (8) from results of static indentation experiments on silicon nitride. Line showing impact kinetic energy U_K estimated by equation (7) is also included for comparison, where m_p is mass of the projectile.

constancy condition of ball projectile that must result in a change of projectile geometry from a perfect original spherical condition (as assumed here) to a more realistic nonspherical one to accommodate the increase in deformed volume. Nevertheless, the U_{KP} approach seems to give at least a first-order approximation of impact energy in the region of small projectile deformation, $d_o < 1.3$ mm (or $V < 300$ m/s). More elaborate analysis of plastic deformation behavior of ball projectile considering the volume constancy condition would give a better estimation of impact energy, a detailed mode of deformation, and the associated strain energy.

Consideration of Back-Side Cracking

Analytical approach.—As stated previously in the section **Impact Morphology and Fractography,** well-developed back-side cracking was observed on the reverse side of the disk at a point just opposite to the impact site starting at impact velocities of 160 and 220 m/s for SN282 and AS800, respectively. A similar behavior of back-side cracking has been observed for thin disks subjected to projectile impact in which disk specimens were rigidly supported circumferentially on their outer edges (ref. 26). When these specimens are subjected to impact, the front side exhibits typical impact damage, while the reverse side is subjected to tension, giving rise to a maximum tensile stress occurring just opposite of the impact site. If the maximum tensile stress at the reverse side is greater than the strength of the material, back-side cracking may occur and propagate until it arrests to reach an equilibrium condition.

As mentioned in **Experimental Procedures,** the disk specimens in this work were placed on an extra AS800 disk backed by a bulky steel bracket, and their edges were clamped together using two small C-clamps positioned 180° apart. Hence, the specimens were considered to be rigidly supported over their whole area. However, as seen from figure 17, well-developed back-side cracking took place as if the specimens had been supported only over their circumferences. There are two speculations regarding possible reasons for the back-side cracking: It could be attributed to either a dynamic effect or the elastic foundation effect. In a dynamic effect, the stress wave interaction of traveling waves would result in a maximum tensile stress field around the plane and the point just beneath (opposite side of) the impact site. The verification of this hypothesis requires a dynamic finite element analysis with accurate boundary conditions, which is beyond the scope of this current report. The latter speculation, the elastic foundation effect, comes from the idea that although the specimens were rigidly supported, they—because of significant impact force—might act like ones supported on elastic foundation, and any deflection of elastic foundation due to impact results in bending of the specimens, which will cause a tensile stress field on the reverse side of the specimens. The solutions of the elastic foundation effect are very complex and require a detailed elastic spring constant of the foundation that is a combined AS800 and steel bracket in this case.

With some simplifying assumptions, the maximum tensile stress on the back side of the disks occurring upon impact was estimated based on the elastic foundations approach (ref. 27). The following assumptions were made in the analysis:

(1) The pressure developed at any point between the beam and the foundation is proportional to the deflection of the beam at that point (see fig. 24(a)).

(2) The specimen is considered as infinite beam subjected to a concentrated load for a conservative approach.

(3) The impact force acts as a concentrated load.

(4) The impact force estimated based on the quasi-static contact theory (eq. (8)) is applicable for a conservative estimation.
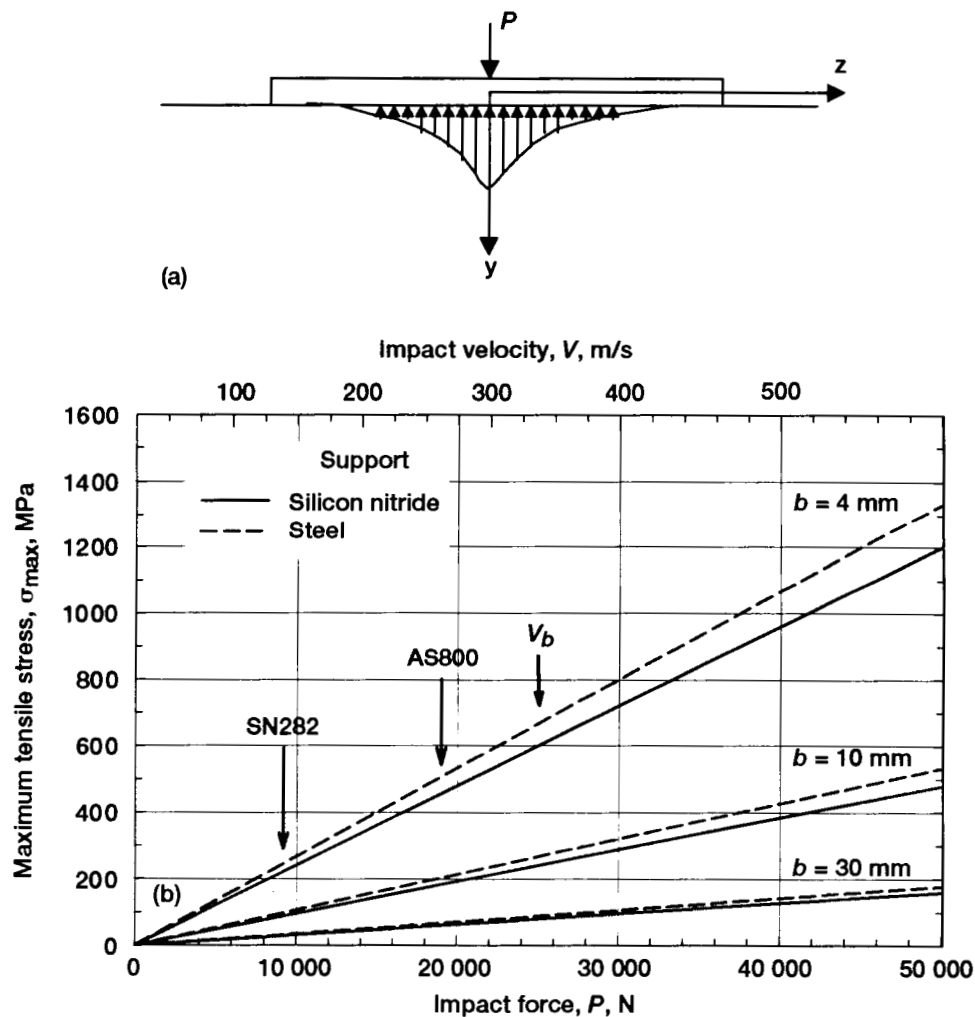
Figure 24.—Elastic foundation of silicon nitride disks during impact testing. (a) Geometry of foundation. (b) Maximum tensile stress occurring on reverse side of disk at point opposite to impact site (which might cause back-side cracking) as function of impact force for different beam widths, b. Estimation was made based on elastic foundation approach (ref. 27). Initiation velocity for back-side cracking is indicated by arrow for each material. V_b is the velocity (350 m/s) that resulted in 100 percent back-side cracking for both silicon nitrides.

The maximum tensile stress σ_{max} occurring in the tension side of the beam opposite to the load point is given with other parameters as follows:

$$\sigma_{max} = \frac{M_{max}c}{I}$$

$$M_{max} = \frac{P}{4\beta}C_{\beta z}$$

$$y = \frac{P\beta}{2k_b}A_{\beta z}$$

$$\beta = \sqrt[4]{\frac{k_b}{4EI}}$$

$$k_b = bk_0 \tag{10}$$

where

$$A_{\beta z} = e^{-\beta z}\left(\sin\beta z + \cos\beta z\right)$$

$$C_{\beta z} = e^{-\beta z}\left(\sin\beta z - \cos\beta z\right) \tag{11}$$

where M_{max} is the maximum bending moment, c is the half of specimen depth, I is the second moment of inertia of a beam, y is the beam deflection, k_b is the spring constant over the width of the foundation, k_0 is the spring constant of foundation, and b is the beam width. The maximum bending moment (and thus stress and deflection) occurs at the load point, i.e., $z = 0$; hence, $A_{\beta z} = C_{\beta z} = 1.0$. Two different elastic supports of silicon nitride ($E = 300$ GPa) and steel ($E = 200$ GPa) disks, placed on an infinitely rigid body, were considered in this estimation. The spring constants of the elastic supports were taken as $k_0 = 2\times10^8$ and 1.3×10^8 N/mm for silicon nitride and steel supports, respectively, based on their Young's modulus values and geometry (2-mm thickness and 40-mm diameter). Three different beam widths of $b = 4$, 10, and 30 mm were considered.

The results of maximum tensile stress estimated using equation (12) are shown in figure 24, where the maximum tensile stress was plotted as a function of impact force for three different beam widths and two different types of elastic supports. The maximum tensile stress is a linear function of impact force and is inversely proportional to specimen width. For $b = 10$ mm, smaller than target specimen's diameter, the maximum tensile stresses at $P = 25$ kN that correspond to the case ($V_b = 350$ m/s) where all AS800 and SN282 disks exhibited back-side cracking (see fig. 18), were 240 and 270 MPa, respectively, for silicon nitride and steel supports. For $b = 30$ mm, which might better represent the actual target specimen diameter, the respective maximum tensile stresses were 80 and 90 MPa. Hence, the estimated maximum tensile stress based on the elastic foundation approach was much lower than the target material's strength and consequently, insufficient to cause back-side cracking. Although several simplifying assumptions were used in the estimation, and their justification must be verified, the elastic foundation approach gives an insight into the reason for the occurrence of back-side cracking at least quantitatively. The back-side cracking was also observed recently for rigidly supported intermetallic disks such as MoSiB and NbSi, subjected to impact by steel ball projectiles of 1.56 mm diameter (Nathal, M.V.; and Draper, S.L.: Ballistic Impact Response of Advanced Silicide Alloys in the IHPTET Program—Preliminary Report. Unpublished work, NASA Glenn Research Center, Cleveland, OH, 2002.)

Consideration of potential component strength and/or reliability with back-side cracking.—As can be seen in the results of back-side cracking, the size of back-side cracks ranged approximately from $a = 5$ to 7 mm (see fig. 18). There were examples of specimens tested at low to intermediate impact velocities where the size of strength-controlling cracks was small, and the resulting postimpact strength was
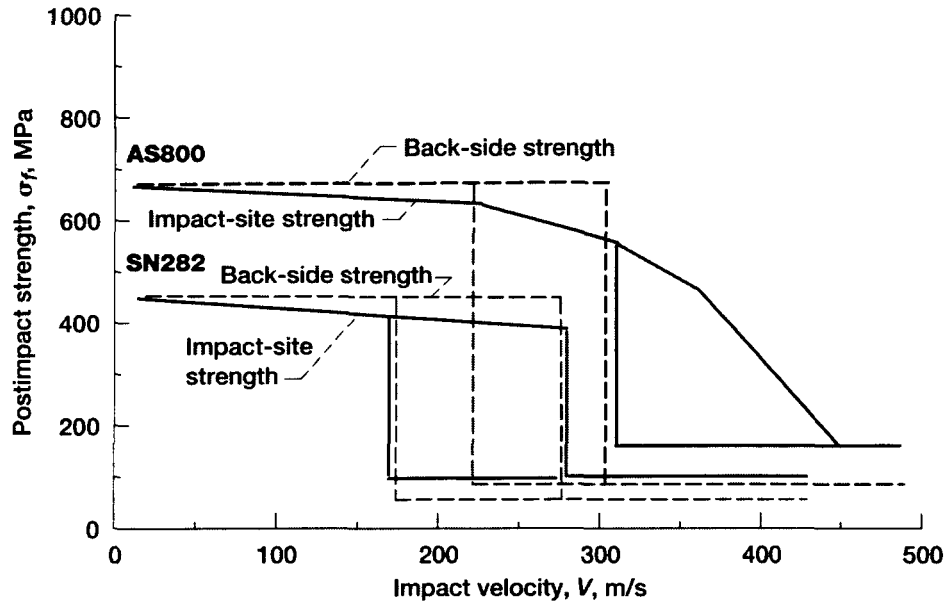
Figure 25.—Postimpact strength as function of impact velocity determined by considering postimpact and back-side strengths of AS800 and SN282 silicon nitrides disks impacted by 1.59-mm-diameter steel ball projectiles at ambient temperature. Solid line represents regular postimpact strength; dashed line, back-side strength.

relatively high, exhibiting significant back-side cracking. Some additional AS800 specimens were flipped over for strength testing so that the back-side cracking was now subjected to tension. The resulting strength was found to be around 120 MPa. If the specimens were regarded as actual structural components under service with unexpected, varying load conditions, the strength and/or reliability of the components, as a consequence, should be based on the degree of severity of back-side cracking. The strength of each of AS800 and SN282 disks containing back-side cracks with an average size of 6 mm, called back-side strength, was estimated to be about 130 and 90 MPa, respectively, using the semicircular assumption. Figure 25 compares strength at the impact site with back-side strength for both silicon nitrides. Back-side cracking initiates with a low probability of occurrence at 160 and 220 m/s for SN282 and AS800, respectively, and it reaches to a 100 percent probability at a velocity of $V \geq 300$ m/s for both silicon nitrides (as already seen in fig. 18). From a structural design point of view, the lower limit of impact velocities should be decreased to 220 m/s for AS800 because of the influence of back-side cracking, whereas it remains unchanged for SN282. Also, the critical impact velocity, where target specimens would exhibit 100 percent back-side cracking, should be decreased from 440 to 300 m/s for AS800.

Fracture Map

As mentioned in the **Impact Morphology and Fractography** section, several different types of damage and/or cracking including ring, radial, cone, and back-side cracks were generated in disk target specimens individually or simultaneously, depending on impact velocity. Figure 26 shows a fracture map, which summarizes the types of damage and/or cracks with respect to impact velocity for both AS800 and SN282 silicon nitrides based on the results of impact morphologies and fractography. For each material at its respective low impact velocities, the occurrence of ring cracks was dominant. At intermediate velocities, ring with either radial or cone (a rare case) cracks are prevalent. Either ring or radial cracks
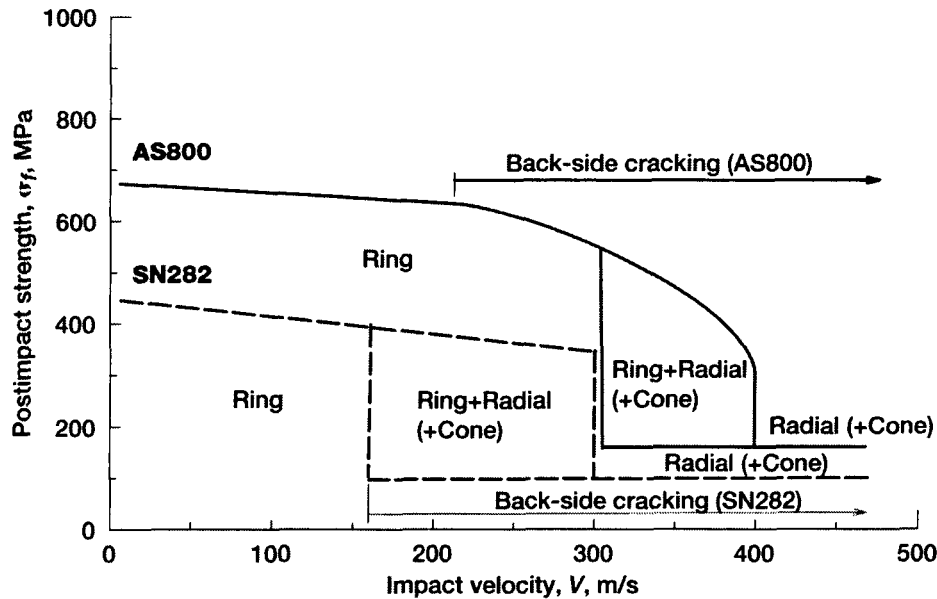
Figure 26.—Fracture map for AS800 and SN282 silicon nitride disks impacted by 1.59-mm-diameter steel ball projectiles at ambient temperature. Range of impact velocity for back-side cracking is also included. "(+Cone)" represents cone cracking not associated with strength-controlling flaws.

determine the postimpact strength depending on the impact velocity, with radial cracking becoming the dominant influence as impact velocity increases. At or above the critical impact velocities, both well-developed radial and cone cracks occur; however, radial cracks uniquely control the postimpact strength.

Figure 26 also includes the range of impact velocities where back-side radial cracking for each silicon nitride takes place. Cone cracking started to develop at intermediate velocities and was very well developed at or above the critical impact velocity. Although cone cracks would not affect component strength significantly in view of their geometry and size compared with the severity of radial cracks, they are responsible for material loss when the cones are formed through the thickness of a component and then separated from the component. This problem would be significant if one of the requirements of the component is some type of sealing, separation, and/or environmental barriers.

Analytical Considerations of Strength Degradation

A phenomenological model of strength degradation due to ball impact was proposed previously by Wiederhorn and Lawn (ref. 1), based on assumptions that the impact event was elastic and quasi-static and that strength degradation was attributed to the formation of cone cracks. Also, another important assumption was that the size for strength-controlling flaws to be effective was proportional to the base radius of the cone (refs. 1, 5, and 9). This latter simplification was based on the fact that the stress intensity factor solution of a cone crack was not available and that the geometry of a cone crack system varied with projectile, target materials, and impact conditions (velocity), etc. With those assumptions, strength degradation was modeled using Hertzian contact analysis, the principle of energy conservation, and indentation fracture relations. The model, despite several assumptions, was in good agreement with experimental data determined for glass impacted by steel or tungsten carbide spherical projectiles (ref. 1). The resulting strength degradation as a function of impact velocity is expressed as follows (ref. 1):

$$\sigma_f = \Phi\left(\frac{k}{E}\right)^{2/15} \rho^{-1/5} R^{-2/3} K_{Ic}^{4/3} V^{-2/5} \tag{12}$$

where Φ is a parameter associated with the projectile geometry. Equation (14) can also be expressed in terms of impact kinetic energy (U_K) in equation (7) to yield

$$\sigma_f = \Phi'\left(\frac{k}{E}\right)^{2/15} R^{-1/15} K_{Ic}^{4/3} U_K^{-1/5} \tag{13}$$

where $\Phi' = (2\pi/3)^{1/5} \Phi$. For a given target material and given material and geometry of a projectile, the postimpact strength depends on [impact velocity]$^{-2/5}$ or [impact kinetic energy]$^{-1/5}$ as seen from equations (14) and (15), respectively.

The postimpact strength (log σ_f) data from figure 6 were plotted as a function of impact kinetic energy (log U_K) in figure 27 based on equation (15). It is noted from figure 27 that the discrepancy in slope between the prediction of $-1/5$[2] and the experimental data seemed insignificant at impact energy of $U_K < 0.8$ J ($V < 300$ m/s) for both AS800 and SN282, except for the lower strength regime of SN282. However, the discrepancy was significant above $U_K > 0.8$ J for AS800 at the higher strength regime while it was already significant at the lower strength regime for SN282, i.e., $V \geq V_c$. The strength degradation model (eq. (14) or (15)) assumed that cone cracks are dominant strength-controlling flaws. However, as seen in this work (e.g., see the fracture map in fig. 26), cone cracking was not uniquely involved in
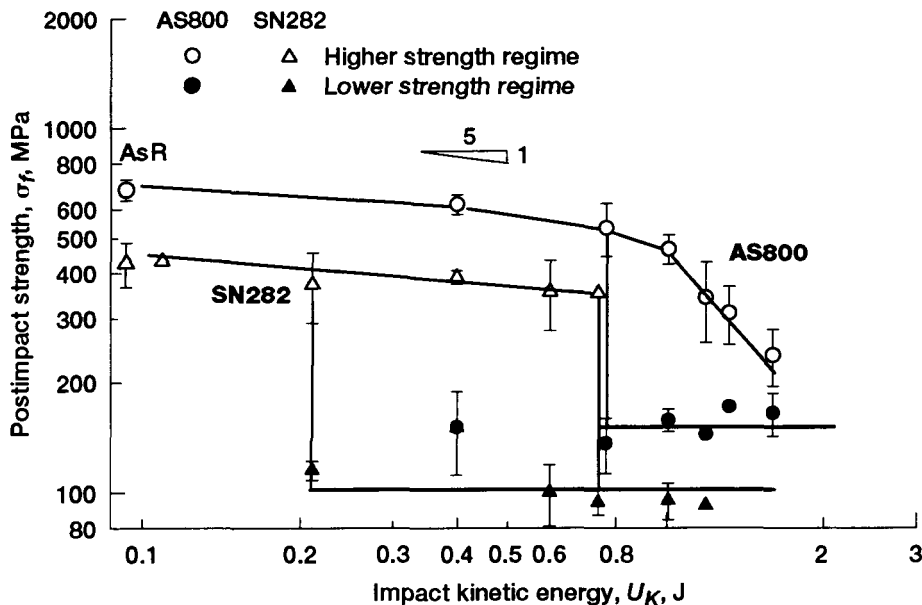

Figure 27.—Postimpact strength as function of impact kinetic energy for AS800 and SN282 silicon nitride disks impacted by 1.59-mm-diameter steel ball projectiles at ambient temperature. Slope of 1/5 indicates theoretical value based on equation (15). Error bars indicate ±1.0 standard deviation. "AsR" indicates as-received biaxial flexure strength of each material.

[2]It has been shown that postimpact strength of brittle materials depends on $U_K^{-1/5}$ and $U_K^{-2/9}$ for blunt (ball) projectiles (cone cracking) and sharp-particle projectiles (radial cracking), respectively (refs. 1 and 2). The use of the impact force versus impact velocity data estimated by the results of the static indentation experiments showed a strength dependency of $U_K^{-4/15}$. These slopes are basically the same ranging from 0.20 to 0.27, indicative of the inappropriateness of the models that consider only one type (either cone or radial) of cracking as a unique strength-controlling flaw configuration.

impact event; rather, several different types of flaws were associated individually or simultaneously, depending on impact velocity. Hence, the cone-cracking model, equation (14) or (15), would not be appropriate to describe the postimpact biaxial strength behavior of AS800 and SN282 silicon nitrides, as also observed previously from uniaxial flexure beam target specimens (refs. 11 and 12). Part of the reason comes from the significant plastic deformation of a projectile upon impact, deviating remarkably from the model's assumption of idealized elastic impact. The complex nature of cracking behavior and the considerable plastic deformation of projectiles encountered in this work would be the most hindering factors to develop a unified strength degradation model in a wide range of impact velocities. This again gives one a precaution that a routine use of any software and/or programs available would never be made without a sound understanding of failure and/or deformation behavior associated with a particular impact event. Furthermore, because of the inherent scatter of postimpact strength caused by different types of damage/cracking generated, use of only a few specimens at a given impact velocity might result in a serious misinterpretation on overall impact behavior and hence should be avoided.

Key Material Parameter of FOD Resistance

Although the model does not predict the postimpact strength behavior over a wide range of impact energy, it is able to determine a key material parameter to affect the resistance to FOD (refs. 11 and 12). For most silicon nitrides, elastic modulus (E), hardness, density, and Poisson's ratio (v) are quite similar. For a given projectile, impact velocity, and given target specimen geometry, the postimpact strength, according to equation (14) or (15), depends on the fracture toughness of a target material with a relation of $\sigma_f \propto (K_{Ic})^{4/3}$. This leads to a simple expression of the postimpact strength ratio between AS800 and SN282 silicon nitrides as follows

$$\frac{\sigma_f \text{ (AS800)}}{\sigma_f \text{ (SN282)}} = \left[\frac{K_{Ic} \text{ (AS800)}}{K_{Ic} \text{ (SN282)}} \right]^{4/3} \tag{14}$$

Use of this relation together with the values of fracture toughness (see table I) determined for both AS800 and SN282 yielded a postimpact strength of AS800 that was 1.68 times greater than that of SN282. The actual strength ratios at 220 and 300 m/s (the only available velocities for comparison) were found to be 1.6 and 1.5, respectively, resulting in good agreement. It would be reasonable to conclude that a silicon nitride with greater fracture toughness can possess greater FOD resistance than another silicon nitride with lower fracture toughness, as also seen in the previous study with flexure bar specimens (refs. 11 and 12). In the previous study (refs. 11 and 12), the key material parameter, fracture toughness, was investigated more extensively using an additional conventional, equiaxed, fine-grained silicon nitride (NC132), as summarized in figure 28; critical impact velocity was studied as a function of fracture toughness (ref. 12). The general trend is manifest from the figure that critical impact velocity increases with increasing fracture toughness, leading to the conclusion that fracture toughness is a key material parameter affecting FOD resistance in silicon nitrides. This is also understandable if one considers that fracture toughness is a measure of resistance to crack initiation and propagation.

Comparison in FOD Behavior Between Blunt (Ball) Projectile and Sharp-Particle Impact

A comparison of postimpact biaxial strength of silicon nitrides between blunt steel ball impact (this study) and sharp SiC-particle (16 and 46 grit) impact (ref. 3 and Choi, S.R.; Ritter, J.E.; and Jakus, K.: Erosion and Impact Behavior of Various Advanced Ceramics at Ambient and Elevated Temperatures. Unpublished work, University of Massachusetts, Amherst, MA, 1988) is shown in figure 29. Note a considerable strength degradation for the case of sharp particle impact occurring even at much lower
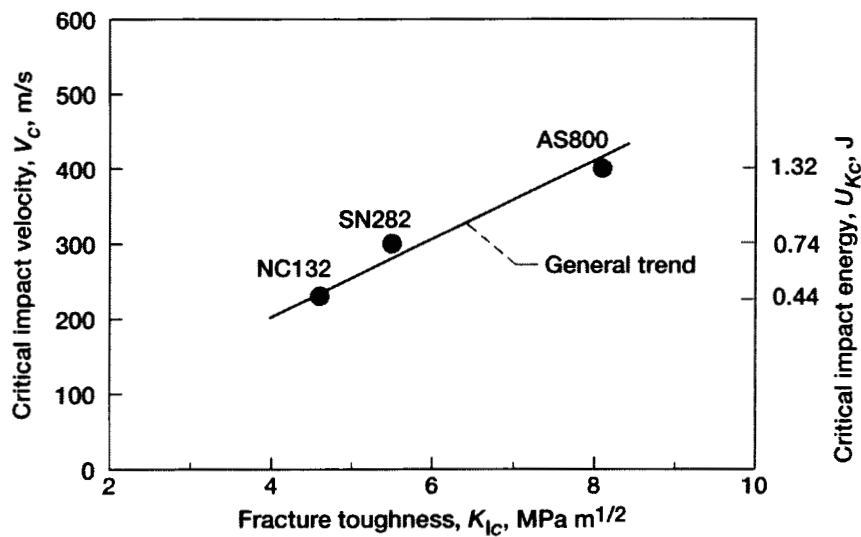
Figure 28.—General trend of critical impact velocity as function of fracture toughness for AS800 and SN282 and one equiaxed fine-grained NC132 (ref. 12) silicon nitride flexure bar specimens.
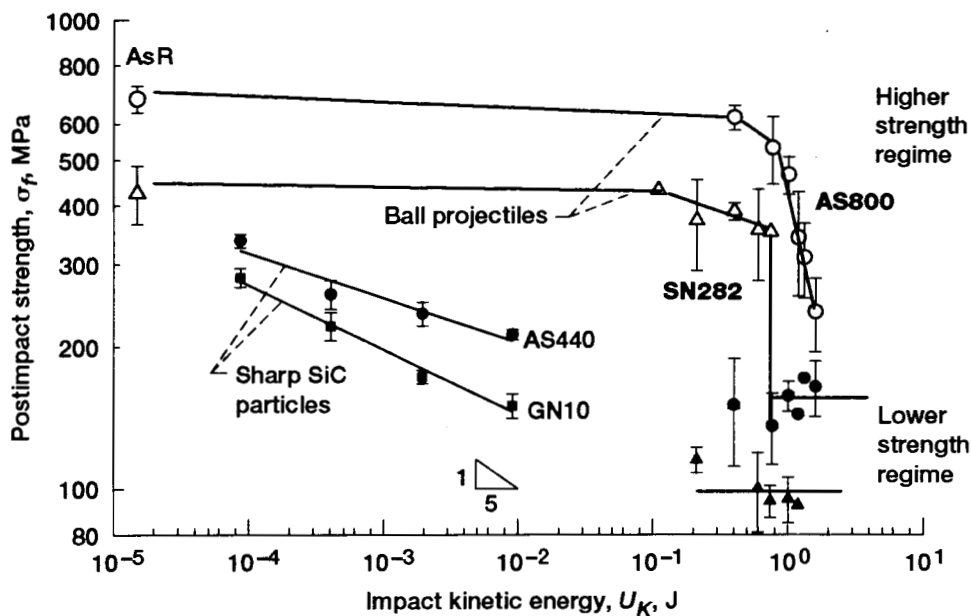

Figure 29.—Comparison of postimpact biaxial strength as function of impact kinetic energy between sharp SiC particle impact for AS440 and GN10 silicon nitride disks (refs. 3 and Choi, S.R.; Ritter, J.E.; and Jakus, K.: Erosion and Impact Behavior of Various Advanced Ceramics at Ambient and Elevated Temperatures. Unpublished work, University of Massachusetts, Amherst, MA, 1988) and blunt steel ball projectile impact (present study) at ambient temperature. "AsR" indicates as-received biaxial fracture strength of both AS800 and SN282 silicon nitride disks. Error bars indicate ±1.0 standard deviation.

impact kinetic energy, showing that the severity of impact damage was far greater in "sharp" particle impact than in "blunt" (steel ball) projectile impact. The sharp particle impact typically produced radial cracks emanating from the impact sites (similar to the Vickers indent cracks that originate from the corners of an impression site), thereby resulting in significant strength degradation. It should be noted that in the sharp-particle studies, fracture toughness of AS440 silicon nitride was greater (by about 30 percent) than that of GN10 silicon nitride; hence, as expected, postimpact strength in sharp-particle impact was greater for AS440 than for GN10. The results in figure 29 show again that for a given target material and a given impact energy, the geometry and material of projectiles are very important parameters affecting the postimpact strength behavior of advanced ceramics.

Comparison in FOD Behavior Between Disks and Flexure Bars

Figure 30 shows a comparison of postimpact strength behaviors between the biaxial disks (2-mm thickness and 45-mm diameter) in this work and the uniaxial flexure bars (4 by 3 by 45 mm in width, depth, and length, respectively) in the previous work (refs. 11 and 12). Both disks and flexure bars were rigidly supported, and the same steel ball projectiles were used. The overall postimpact strength was higher for uniaxial flexure bars than for biaxial disks because of the size effect.[3] The critical impact
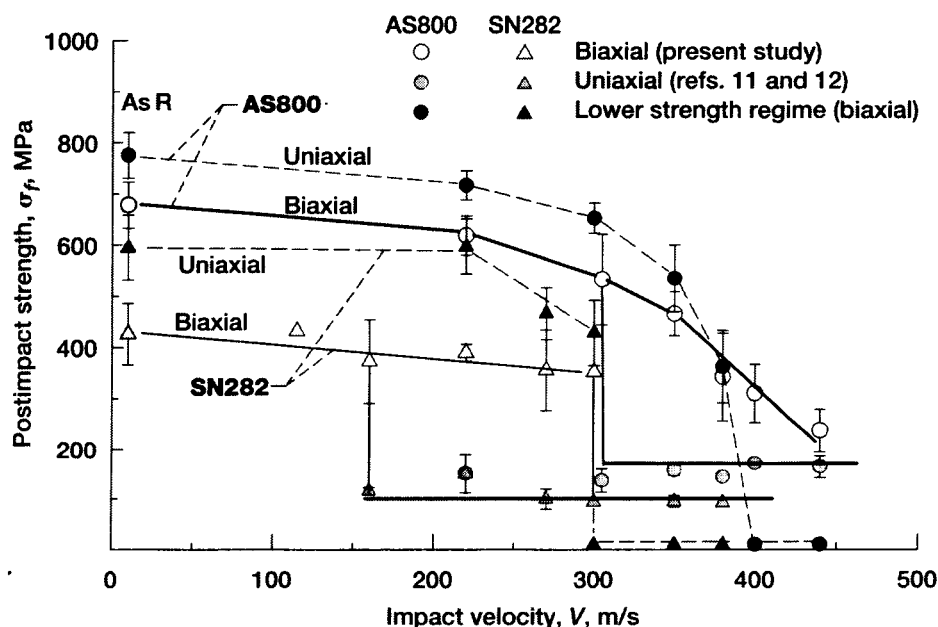

Figure 30.—Comparison of postimpact strength as function of impact velocity between flexure bars (refs. 11 and 12) and biaxial disks (present study) of AS800 and SN282 silicon nitrides impacted by 1.59-mm-diameter steel ball projectiles at ambient temperature. "AsR" indicates as-received fracture strength. Error bars indicate ±1.0 standard deviation.

---

[3] A prediction of strength from one specimen configuration (uniaxial) to another (biaxial) was made using the principle of independent action (PIA, Weibull statistics) with surface flaws for as-received specimens. The ratio of predicted biaxial to uniaxial strengths (as-received) was 0.90 and 0.82 for AS800 and SN282, respectively, whereas the ratio of actual biaxial and uniaxial strengths was found to be 0.89 and 0.72. From excellent to reasonable agreement was found for AS800 and SN282 specimens, respectively. The Weibull moduli in this prediction were taken as $m = 20$ and 10 for AS800 and SN282, respectively.

velocity for uniaxial bars was $V_c \approx 300$ and 400 m/s for SN282 and AS800, respectively, while for biaxial disks it was $V_c \approx 300$ and 440 m/s, resulting basically in good agreement in V_c between the two different specimen configurations. However, the lower strength regime uniquely occurring in biaxial disks was not seen in uniaxial flexure bars, primarily due to the difference in specimen thickness: thin (disks) versus thick (flexure bars). Furthermore, the back-side cracking characterizing biaxial disks was not exhibited in the flexure bars, possibly again due to the difference in specimen thickness, as noted by the elastic foundation approach (with strength depending on $[1/(\text{thickness})^2]$). Although the general trend of postimpact strength with respect to impact velocity seemed similar in both specimen configurations, the occurrence of significant radial and back-side cracking was very different from one specimen configuration to another even using the same target material under the same impact conditions. This implies that a particular set of impact data generated under particular impact conditions may not be universally applicable to a variety of applications. A case-by-case approach must be sought.

Other Considerations

Designing aeroengine components to withstand FOD events is a complex task. Consideration of many factors is required, both in the generation of FOD data as well as in actual component design efforts. A sample of these numerous factors includes the following:

(1) Effect of projectile material and geometry
(2) Effect of test specimen material and geometry
(3) Effect of test-specimen support and component attachment
(4) Effect of temperature and environment
(5) Appropriate protective coatings
(6) Geometrical design of components to enhance FOD resistance
(7) FOD, reliability, and life prediction codes

Not only must each of these factors be scrutinized individually, but the effects of interactions between multiple factors also must be considered. Notwithstanding the immense challenges this poses, a strategy for mitigating FOD damage must be developed and employed in order to achieve the most desirable performance of components in service. Hence, some of these factors are immediate subjects of study and the related work is under way, such as in the tasks discussed in this report. Others are long-term efforts and are pursued continually in the quest for improving the efficiency and reliability of aeroengine components.

Conclusions

Based on the results of FOD testing using biaxial disks at ambient temperature for two in situ toughened, gas-turbine-grade silicon nitrides (AS800 and SN282), following conclusions were made:

1. The overall resistance—estimated by postimpact strength—to foreign object damage (FOD) by steel ball projectiles with a diameter of 1.59 mm was found to be greater for AS800 silicon nitride than for SN282 silicon nitride in an impact velocity range from 115 to 440 m/s.

2. The critical impact velocities, in which biaxial disk target specimens exhibited the lowest postimpact strength, were about 440 and 300 m/s, respectively, for AS800 and SN282 silicon nitrides. The occurrence of critical impact velocity was associated with the generation of significant sizes (5 to 7 mm) of radial cracks originating from the impact sites.

3. The difference in FOD resistance between AS800 and SN282 silicon nitrides was primarily due to the difference in fracture toughness, as also observed previously in flexure bar specimens of AS800 and SN282 silicon nitrides and a fine-grain NC132 silicon nitride (ref. 12).

4. As impact velocity increased, more different crack types were involved in the impact event, occurring either individually or simultaneously. A fracture map was proposed to identify the occurrence of particular crack systems including ring, radial, cone, and back-side cracking with respect to impact velocity.

5. In terms of the different specimen geometries and configurations, the degree of additional damage by radial and back-side cracking was much more severe in thin biaxial specimens than in thick uniaxial flexure bars. This indicates that a particular set of impact data generated under particular impact conditions may not be universally applicable to a variety of applications. A case-by-case approach to specific geometries and configurations should be taken into consideration.

References

1. Wiederhorn, S.M.; and Lawn, B.R.: Strength Degradation of Glass Resulting from Impact with Spheres. J. Am. Ceram. Soc., vol. 60, no. 9–10, 1977, pp. 451–458.

2. Wiederhorn, S.M.; and Lawn, B.R.: Strength Degradation of Glass Impacted with Sharp Particles: I, Annealed Surfaces. J. Am. Ceram. Soc., vol. 62, no. 1–2, 1979, pp. 66–70.

3. Ritter, J.E., et al.: Effect of Microstructure on the Erosion and Impact Damage of Sintered Silicon Nitride. J. Mater. Sci., vol. 26, no. 20, pp. 5543–5546.

4. Akimune, Yoshio; Katano, Yasushi; and Matoba, Kazuo: Spherical-Impact Damage and Strength Degradation in Silicon Nitrides for Automobile Turbocharger Rotors. J. Am. Ceram. Soc., vol. 72, no. 8, 1989, pp. 1422–1428.

5. Knight, C.G.; Swain, M.V.; and Chaudhri, M.M.: Impact of Small Steel Spheres on Glass Surfaces. J. Mater. Sci., vol. 12, no. 8, 1977, pp. 1573–1586.

6. Rajendran, A.M.; and Kroupa, J.L.: Impact Damage Model for Ceramic Materials. J. Appl. Phys., vol. 66, no. 8, 1989, pp. 3560–3565.

7. Taylor, L.M.; Chen, E.P.; and Kuszmaul, J.S.: Microcrack-Induced Damage Accumulation in Brittle Rock Under Dynamic Loading. Comp. Methods Appl. Mech. Eng., vol. 55, no. 3, 1986, pp. 301–320.

8. Mouginot, R.; and Maugis, D.: Fracture Indentation Beneath Flat and Spherical Punches. J. Mater. Sci., vol. 20, no. 12, 1985, pp. 4354–4376.

9. Evans, A.G.; and Wilshaw, T.R.: Dynamic Solid Particle Damage in Brittle Materials: An Appraisal. J. Mater. Sci., vol. 12, no. 1, 1977, pp. 97–116.

10. Liaw, B.M.; Kobayashi, A.S.; and Emery, A.F.: Theoretical Model of Impact Damage in Structural Ceramics. J. Am. Ceram. Soc., vol. 67, no. 8, 1984, pp. 544–548.

11. Choi, Sung R., et al.: Foreign Object Damage of Two Gas-Turbine Grade Silicon Nitrides at Ambient Temperature. Ceram. Eng. Sci. Proc., vol. 23, issue 3, 2002, pp. 193–202.

12. Choi, Sung R., et al.: Foreign Object Damage Behavior of Two Gas-Turbine Grade Silicon Nitrides by Steel Ball Projectiles at Ambient Temperature. NASA/TM—2002-211821, 2002. http://gltrs.grc.nasa.gov/cgi-bin/GLTRS/browse.pl?2002/TM-2002-211821.html

13. Ohji, Tatsuki: Long Term Tensile Creep Behavior of Highly Heat-Resistant Silicon Nitride for Ceramic Gas Turbines. Ceram. Eng. Sci. Proc., vol. 22, issue 3, 2001, pp. 159–166.

14. Lofaj, František, et al.: Tensile Creep in the Next Generation Silicon Nitride. Ceram. Eng. Sci. Proc., vol. 22, issue 3, 2001, pp. 167–174.

15. Lin, H.T., et al.: Evaluation of Creep Property of AS800 Silicon Nitride From As-Processed Surface Regions. Ceram. Eng. Sci. Proc., vol. 22, issue 3, 2001, pp. 175– 82.

16. Choi, S.R.; and Gyekenyesi, J.P.: Elevated-Temperature "Ultra" Fast Fracture Strength of Advanced Ceramics: An Approach to Elevated-Temperature "Inert" Strength. J. Eng. Gas Turbines Power, vol. 121, no. 1, 1999, pp. 18–24.

17. Choi, S.R.; and Gyekenyesi, J.P.: 'Ultra'-Fast Strength of Advanced Structural Ceramics at Elevated Temperatures. Fracture Mechanics of Ceramics, Vol. 13, R.C. Bradt, et al., eds., Kluwer Academic/Plenum Publishers, New York, NY, 2002, pp. 27– 46.

18. Choi, S.R.; and Gyekenyesi, J.P.: Slow Crack Growth Analysis of Advanced Structural Ceramics Under Combined Loading Conditions: Damage Assessment in Life Prediction Testing. J. Eng. Gas Turbines Power, vol. 123, no. 2, 2001, pp. 277–287.

19. Standard Test Method for Flexural Strength of Advanced Ceramics at Ambient Temperature. Annual Book of ASTM Standards 2002, ASTM Designation: C 1161–94 (Reapproved 1996), section 15, vol. 15.01, ASTM, West Conshohocken, PA, 2002.

20. Standard Test Method for Dynamic Young's Modulus, Shear Modulus, and Poisson's Ratio for Advanced Ceramics by Impulse Excitation of Vibration. Annual Book of ASTM Standards 2002, ASTM Designation: C 1259–01, section 15, vol. 15.01, ASTM, West Conshohocken, PA, 2002.

21. Standard Test Method for Vickers Indentation Hardness of Advanced Ceramics. Annual Book of ASTM Standards 2002, ASTM Designation: C 1327–99, section 15, vol. 15.01, ASTM, West Conshohocken, PA, 2002.

22. Standard Test Methods for Determination of Fracture Toughness of Advanced Ceramics at Ambient Temperature. Annual Book of ASTM Standards 2002, ASTM Designation: C 1421–01a, section 15, vol. 15.01, ASTM, West Conshohocken, PA, 2002.

23. Akimune, Yoshio; Akiba, Toru; and Ogasawara, Toshio: Damage Behaviour of Silicon Nitride for Automotive Gas Turbine Use When Impacted by Several Types of Spherical Particles. J. Mater. Sci., vol. 30, no. 4, 1995, pp. 1000–1004.

24. Mecholsky Jun, J.J.; Freimam, S.W.; and Rice, R.W.: Fracture Surface Analysis of Ceramics. J. Mater. Sci., vol. 11, no. 7, 1976, pp. 1310–1319.

25. Choi, Sung R.; and Gyekenyesi, John P.: Crack Branching and Fracture Mirror Data of Glasses and Advanced Ceramics. NASA/TM—1998-206536, 1998. http://gltrs.grc.nasa.gov/cgi-bin/GLTRS/browse.pl?1998/TM-1998-206536.html

26. Hara, Yasushi, et al.: Development and Evaluation of Silicon Nitride Components for Ceramic Gas Turbine. ASME 98–GT–498, 1998.

27. Boresi, Arthur P.: Advanced Mechanics of Materials. Second ed., Wiley, New York, NY, 1952.

Appendix—Symbols

A	contact area
A_b	crack branching constant, defined in eq. (3)
$A_{\beta z}$	parameter defined in eq. (11)
a	radius of contact area
b	beam width
$C_{\beta z}$	parameter defined in eq. (11)
c	half specimen depth
c_f	crack length at fracture
cp	compressive contact pressure
d	contact diameter
d_i	impression inner diameter
d_o	impression outer diameter
E	elastic modulus
F	Failure probability
I	beam second moment of inertia
i	failure location distance from impact center
K_{Ic}	fracture toughness
k	parameter, defined in eq. (2)
k_0	foundation spring constant
k_b	spring constant over width of foundation
M_{max}	maximum bending moment
m	Weibull modulus
m_p	projectile mass
P	impact force
P_s	applied static indent load
R	radius of projectile
r_b	crack branching length
U_K	projectile kinetic energy
U_{Kc}	critical impact energy
U_{KP}	projectile plastic deformation energy
V	impact velocity
V_b	velocity at which back-side cracking starts to occur
V_c	critical impact velocity
Y	crack geometry factor, $Y = \sqrt{\pi}/2$
y	beam deflection
z	deformation depth of ball projectile
α	constant, from eq. (1)
β	parameter defined in equation (10)
ν	Poisson's ratio
ρ	density of projectile
σ_p	compressive flow stress
σ_f	biaxial fracture strength
σ_{max}	maximum tensile stress
σ_θ	characteristic strength
Φ	parameter associated with projectile geometry, from eq. (12)
Φ'	parameter associated with projectile geometry, from eq. (13)

REPORT DOCUMENTATION PAGE

1. AGENCY USE ONLY (Leave blank)	2. REPORT DATE	3. REPORT TYPE AND DATES COVERED
	July 2003	Technical Memorandum

4. TITLE AND SUBTITLE

Foreign Object Damage in Disks of Two Gas-Turbine-Grade Silicon Nitrides by Steel Ball Projectiles at Ambient Temperature

5. FUNDING NUMBERS

WBS-22-708-31-07

6. AUTHOR(S)

Sung R. Choi, J. Michael Pereira, Lesley A. Janosik, and Ramakrishna T. Bhatt

7. PERFORMING ORGANIZATION NAME(S) AND ADDRESS(ES)

National Aeronautics and Space Administration
John H. Glenn Research Center at Lewis Field
Cleveland, Ohio 44135-3191

8. PERFORMING ORGANIZATION REPORT NUMBER

E-13844

9. SPONSORING/MONITORING AGENCY NAME(S) AND ADDRESS(ES)

National Aeronautics and Space Administration
Washington, DC 20546-0001

10. SPONSORING/MONITORING AGENCY REPORT NUMBER

NASA TM—2003-212224

11. SUPPLEMENTARY NOTES

Sung R. Choi, Ohio Aerospace Institute, Brook Park, Ohio 44142; J. Michael Pereira, Lesley A. Janosik, and Ramakrishna T. Bhatt, NASA Glenn Research Center. Responsible person, Sung R. Choi, organization code 5920, 216-433-8366.

12a. DISTRIBUTION/AVAILABILITY STATEMENT

Unclassified - Unlimited
Subject Categories: 07 and 39   Distribution: Nonstandard

Available electronically at http://gltrs.grc.nasa.gov

This publication is available from the NASA Center for AeroSpace Information, 301-621-0390.

12b. DISTRIBUTION CODE

13. ABSTRACT (Maximum 200 words)

Foreign object damage (FOD) behavior of two commercial gas-turbine-grade silicon nitrides, AS800 and SN282, was determined at ambient temperature through postimpact strength testing of disks impacted by steel ball projectiles with a diameter of 1.59 mm in a velocity range from 115 to 440 m/s. AS800 silicon nitride exhibited a greater FOD resistance than SN282, primarily due to its greater value of fracture toughness (K_{Ic}). The critical impact velocity V_c for which the corresponding postimpact strength was the lowest was $V_c \approx 440$ and 300 m/s for AS800 and SN282, respectively. A unique lower strength regime was typified for both silicon nitrides depending on impact velocity and was attributed to significant radial cracking. The damage generated by projectile impact was typically in the form of ring, radial, and cone cracks with their severity and combination being dependent on impact velocity. Unlike the thick (4 mm) flexure bar specimens used in our previous studies, the thin (2 mm) disk target specimens exhibited a unique back-side radial cracking on the reverse side just beneath the impact sites at and above impact velocities of 160 m/s for SN282 and 220 m/s AS800.

14. SUBJECT TERMS

Foreign object damage; FOD; Turbine-grade silicon nitrides; Impact testing; Strength testing; Mechanical testing for ceramics; Strength degradation due to FOD

15. NUMBER OF PAGES

39

16. PRICE CODE

17. SECURITY CLASSIFICATION OF REPORT	18. SECURITY CLASSIFICATION OF THIS PAGE	19. SECURITY CLASSIFICATION OF ABSTRACT	20. LIMITATION OF ABSTRACT
Unclassified	Unclassified	Unclassified	